

Nanoscale Spin Injector Driven by a Microwave Voltage

A.I. Nikitchenko[✉] and N.A. Pertsev^{✉*}

Ioffe Institute, St. Petersburg 194021, Russia



(Received 12 May 2020; revised 17 July 2020; accepted 14 August 2020; published 9 September 2020)

We propose an electrically driven spin injector into normal metals and semiconductors, which is based on a magnetic tunnel junction (MTJ) subjected to a microwave voltage. Efficient functioning of such an injector is provided by electrically induced magnetization precession in the “free” layer of MTJ, which generates the spin pumping into a metallic or semiconducting overlayer. To validate the feasibility of the proposed device, we theoretically describe the spin and charge dynamics in the $\text{Co}_{20}\text{Fe}_{60}\text{B}_{20}/\text{MgO}/\text{Co}_{20}\text{Fe}_{60}\text{B}_{20}/\text{Au}$ and $\text{Co}_{20}\text{Fe}_{60}\text{B}_{20}/\text{MgO}/\text{Co}_{20}\text{Fe}_{60}\text{B}_{20}/\text{GaAs}$ tunneling heterostructures. First, the magnetization dynamics in the free $\text{Co}_{20}\text{Fe}_{60}\text{B}_{20}$ layer is quantified with the account of a spin-transfer torque generated by the spin-polarized current flowing through the MTJ and a voltage-controlled magnetic anisotropy associated with the $\text{Co}_{20}\text{Fe}_{60}\text{B}_{20}-\text{MgO}$ interface. The calculations are performed in the macrospin approximation for an ultrathin $\text{Co}_{20}\text{Fe}_{60}\text{B}_{20}$ layer with perpendicular anisotropy and nanoscale in-plane dimensions. By numerically solving the Landau-Lifshitz-Gilbert-Slonczewski equation, we determine dependences of the precession amplitude on the frequency f and magnitude V_{\max} of the ac voltage applied to the MTJ. It is found that the frequency dependence changes drastically above the threshold amplitude $V_{\max} \approx 200$ mV, exhibiting a break at the resonance frequency f_{res} due to nonlinear effects. The results obtained for the magnetization dynamics are then used to describe the spin injection and pumping into the Au and GaAs overlayers. The total spin-current density near the interface is calculated as a function of time at different excitation frequencies and voltage amplitudes. Since the generated spin current creates additional charge current owing to the inverse spin Hall effect, we also calculate distributions of the charge-current density and electric potential in the thick Au overlayer. The calculations show that the arising transverse voltage, which can be used to probe the efficiency of spin generation electrically, becomes experimentally measurable at $f = f_{\text{res}}$. Finally, we evaluate the spin accumulation in a long n^+ -GaAs bar coupled to the MTJ and determine its temporal variation and spatial distribution along the bar. It is found that the ac spin accumulation under resonant excitation is large enough for experimental detection via a voltage between two ferromagnetic nanocontacts even at micrometer distances from the MTJ. This result demonstrates high efficiency of the described nanoscale spin injector driven by microwave voltage.

DOI: [10.1103/PhysRevApplied.14.034022](https://doi.org/10.1103/PhysRevApplied.14.034022)

I. INTRODUCTION

Efficient spin injectors are necessary for the functioning of various spintronic devices, such as spin diodes, spin field-effect transistors, magnetic bipolar transistors, hot-electron spin transistors, and spin-based logic gates [1,2]. The key element of such injectors is a ferromagnet providing a spin imbalance in a neighboring normal metal or semiconductor. In all-metallic heterostructures, the spin imbalance can be achieved by simply injecting a spin-polarized current from the ferromagnetic emitter into a paramagnetic or diamagnetic metal [3,4]. However, this direct spin injection becomes inefficient for semiconductors due to an impedance mismatch at the interface [5]. The problem can be solved by inserting of a tunnel

barrier at a ferromagnet-semiconductor interface, as predicted theoretically [6] and demonstrated experimentally at room temperature for a $\text{Co}_{70}\text{Fe}_{30}-\text{MgO}$ tunnel injector into GaAs [7]. However, the injected spin-polarized carriers are hot, whereas cold-electron spin injection is desirable for semiconductor devices [8].

Another method to create a spin current and spin accumulation in a normal conductor is based on the spin pumping generated by a ferromagnet with precessing magnetization [8]. When the precessing metallic ferromagnet is brought into Ohmic contact with the conductor, it represents a “spin battery,” which becomes effective at the ferromagnetic resonance [9]. Efficient spin pumping into various normal metals has been achieved with the aid of metallic and insulating ferromagnetic films excited by microwave magnetic fields [10–14]. Room-temperature generation of spin flow in semiconductors through both Ohmic and Schottky contacts was demonstrated by this

*pertsev.domain@mail.ioffe.ru

technique as well [15,16]. However, the use of microwave magnetic fields has serious disadvantages for practical applications, such as associated high-energy losses and issues related with the downscaling of spintronic devices. Fortunately, the magnetization precession can also be excited electrically using spin-polarized currents [17–21], electric-field-dependent magnetic anisotropy [22–25], and piezoelectrically generated elastic waves [26–30], which opens the possibility to develop spin injectors with greatly reduced power consumption.

In this paper, we theoretically study a nanoscale magnetic tunnel junction (MTJ) subjected to a microwave voltage and show that it can be employed as an efficient spin injector into normal metals and semiconductors. To this end, we first describe electrically induced magnetization precession in the “free” layer of a $\text{Co}_{20}\text{Fe}_{60}\text{B}_{20}/\text{MgO}/\text{Co}_{20}\text{Fe}_{60}\text{B}_{20}$ junction with the account of additional damping caused by the spin pumping into a metallic or semiconducting overlayer [31]. The calculations are carried out in the macrospin approximation via numerical integration of the Landau-Lifshitz-Gilbert-Slonczewski (LLGS) equation. Since the spin pumping generated by the precession should intensify with increasing amplitude V_{\max} of the ac voltage applied to the MTJ, our analysis focuses on peculiarities of the magnetization dynamics appearing in the range of enhanced amplitudes V_{\max} , where nonlinear effects become important. The results obtained for the magnetization precession in the free $\text{Co}_{20}\text{Fe}_{60}\text{B}_{20}$ layer are then employed to calculate the spin injection and pumping into an Au overlayer and into a GaAs bar coupled to the MTJ. To evaluate the efficiency of the proposed spin injector, which can be probed electrically [3,11], we also quantify the charge flow and the distribution of electric potential in the Au overlayer and calculate the spin accumulation in the GaAs bar.

II. MAGNETIZATION DYNAMICS DRIVEN BY MICROWAVE VOLTAGE

Magnetic dynamics in MTJs can be generated electrically because a spin-polarized current creates a spin-transfer torque (STT) when the magnetizations of two electrodes are noncollinear [32,33]. Furthermore, in MgO-based MTJs having voltage-controlled magnetic anisotropy (VCMA), magnetization oscillations can be induced in the free layer (FL) by microwave-frequency voltages even in the absence of significant STTs [22, 24,25]. To enhance the STT acting on the FL magnetization, one can employ an MTJ with an ultrathin FL having perpendicular magnetic anisotropy [34,35] and a thick reference layer (RL) with in-plane magnetization (Fig. 1). This feature motivated us to consider such a geometry in our study, where we focus on the $\text{Co}_{20}\text{Fe}_{60}\text{B}_{20}/\text{MgO}/\text{Co}_{20}\text{Fe}_{60}\text{B}_{20}$ junction having pronounced VCMA [23]. It should be noted that, owing

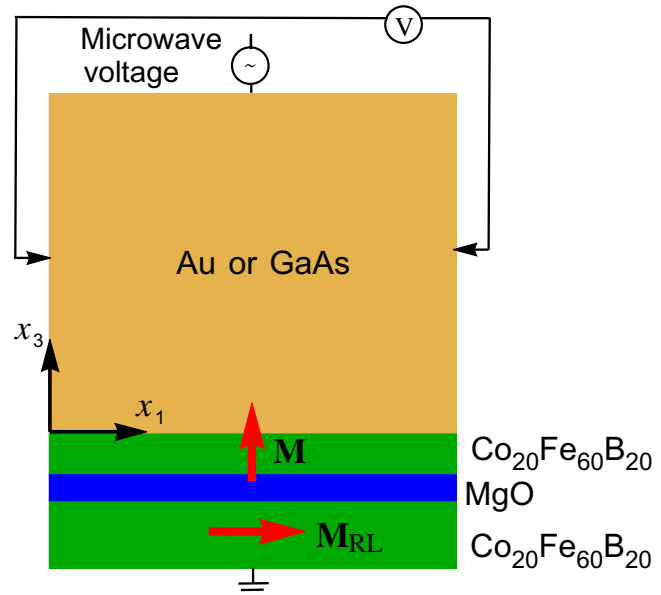


FIG. 1. Design of electrically driven spin injector based on a magnetic tunnel junction subjected to a microwave voltage. The studied heterostructure comprises $\text{Co}_{20}\text{Fe}_{60}\text{B}_{20}/\text{MgO}/\text{Co}_{20}\text{Fe}_{60}\text{B}_{20}$ tunnel junction with an ultra-thin free layer covered by Au or GaAs. Information on the spin injection into the overlayer can be obtained by measuring the voltage V caused by the inverse spin Hall effect with the aid of nanowires brought into contact with opposite lateral sides of the overlayer.

to the interlayer exchange coupling (IEC) between FL and RL, the FL magnetization \mathbf{M} slightly deviates from the perpendicular-to-plane orientation (polar angle $\theta \approx 3^\circ$) even in the absence of applied voltage and external magnetic field. Therefore, the VCMA contributes to the voltage-induced destabilization of the FL magnetization along with the STT [24].

To quantify the magnetization oscillations $\delta\mathbf{M}(t)$ generated by the applied ac voltage $V_{\text{ac}} = V_{\max} \sin(2\pi ft)$ in FL with nanoscale in-plane dimensions, we use the LLGS equation and the macrospin approximation [36], which implies the same magnetization direction $\mathbf{m} = \mathbf{M}/M_s$ in the whole FL and a constant saturation magnetization M_s . RL is assumed to be uniformly magnetized with a fixed magnetization direction \mathbf{m}_{RL} unaffected by the applied voltage, which is confirmed by numerical calculations at the considered RL thickness $t_{\text{RL}} = 3$ nm. Since the fieldlike torque does not change the magnetic dynamics qualitatively [23,37], we write the LLGS equation in the form

$$\frac{d\mathbf{m}}{dt} = -\gamma\mu_0\mathbf{m} \times \mathbf{H}_{\text{eff}} + \alpha\mathbf{m} \times \frac{d\mathbf{m}}{dt} + \frac{\tau_{\text{STT}}}{M_s}\mathbf{m} \times (\mathbf{m} \times \mathbf{m}_{\text{RL}}), \quad (1)$$

where $\gamma > 0$ is the electron's gyromagnetic ratio, μ_0 is the permeability of vacuum, α is the Gilbert dimensionless damping parameter, and \mathbf{H}_{eff} is the effective magnetic field acting on the FL magnetization. The last term in Eq. (1) allows for the STT created by the spin-polarized current flowing across FL, with the factor τ_{STT} being proportional to the applied voltage $V = V_{\text{dc}} + V_{\text{ac}}$ in the first approximation. In the case of elastic tunneling in symmetric MTJs, the theoretical calculations yield $\tau_{\text{STT}} = (\gamma \hbar / 2e)(V G_P / t_{\text{FL}}) \eta / (1 + \eta^2)$, where $e > 0$ is the elementary charge, \hbar is the reduced Planck constant, t_{FL} is the FL thickness, $\eta = \sqrt{(G_P - G_{\text{AP}})/(G_P + G_{\text{AP}})}$ is the MTJ asymmetry factor, and G_P and G_{AP} are the junction's conductances per unit area at parallel and antiparallel electrode magnetizations, respectively [33]. To take into account the influence of the precession-induced spin pumping into a metallic or semiconducting overlayer, we renormalize the parameters γ and α involved in Eq. (1) as [31]

$$\begin{aligned} \alpha &= \frac{\gamma}{\gamma_0} \left(\alpha_0 + \frac{g_L \mu_B}{4\pi M_s t_{\text{FL}}} \text{Re}[g_{\uparrow\downarrow}^r] \right), \\ \frac{1}{\gamma} &= \frac{1}{\gamma_0} \left(1 + \frac{g_L \mu_B}{4\pi M_s t_{\text{FL}}} \text{Im}[g_{\uparrow\downarrow}^r] \right), \end{aligned} \quad (2)$$

where γ_0 and α_0 denote the values of γ and α in the absence of spin pumping, g_L is the Landé factor, μ_B is the Bohr magneton, and $g_{\uparrow\downarrow}^r$ is the complex reflection spin-mixing conductance per unit area of the FL-overlayer contact [38]. Since in our case the numerical estimates demonstrate a negligible dependence of the Gilbert parameter α_0 on the magnetization precession power [39], we consider α_0 as a constant quantity.

For a homogeneously magnetized ultrathin $\text{Co}_{20}\text{Fe}_{60}\text{B}_{20}$ layer, the field $\mathbf{H}_{\text{eff}} = -(\mu_0 M_s)^{-1} \partial F / \partial \mathbf{m}$ involved in Eq. (1) can be determined by differentiating the effective volumetric Helmholtz free-energy density F of that layer. The magnetization-dependent part $\Delta F(\mathbf{m})$ of this energy may be written as

$$\begin{aligned} \Delta F &\simeq K_1(m_1^2 m_2^2 + m_1^2 m_3^2 + m_2^2 m_3^2) + \frac{K_s}{t_{\text{FL}}} m_3^2 \\ &+ \frac{1}{2} \mu_0 M_s^2 (N_{11} m_1^2 + N_{22} m_2^2 + N_{33} m_3^2 \\ &+ 2N_{12} m_1 m_2 + 2N_{13} m_1 m_3 + 2N_{23} m_2 m_3) \\ &- \frac{U_{\text{IEC}}}{t_{\text{FL}}} \mathbf{m} \cdot \mathbf{m}_{\text{RL}}, \end{aligned} \quad (3)$$

where m_i ($i = 1, 2, 3$) are the projections of \mathbf{m} on the crystallographic axes x_i of the $\text{Co}_{20}\text{Fe}_{60}\text{B}_{20}$ layer, which is assumed to be epitaxial with the x_3 axis orthogonal to its surfaces, K_1 characterizes the cubic magnetocrystalline anisotropy of $\text{Co}_{20}\text{Fe}_{60}\text{B}_{20}$ [40], K_s defines the total specific energy of the FL surfaces, U_{IEC} is the IEC energy per unit area, N_{ij} are the demagnetizing

factors, and the external magnetic field is absent in our case. Since the magnetic anisotropy associated with the $\text{Co}_{20}\text{Fe}_{60}\text{B}_{20}$ –MgO interface varies with the electric field E_3 created in MgO [35,41], the factor K_s appears to be a voltage-dependent quantity. In the linear approximation supported by first-principles calculations [42] and experimental data [41], $K_s = K_s^0 + k_s V / t_b$, where $K_s^0 = K_s(E_3 = 0)$, $k_s = \partial K_s / \partial E_3$ is the electric field sensitivity of K_s , and t_b is the thickness of the MgO tunnel barrier.

The numerical integration of Eq. (1) is realized with the aid of the projective Euler scheme at a fixed integration step $\delta t = 10$ fs. The computations are performed for the rectangular FL with nanoscale in-plane dimensions $L_1 = 200$ nm and $L_2 = 80$ nm and the thickness $t_{\text{FL}} = 1.69$ nm smaller than the threshold thickness $t_{\text{SRT}} = 1.718$ nm, at which a spin reorientation transition (SRT) to the in-plane magnetization orientation takes place at $V = 0$. The FL demagnetizing factors N_{ii} are calculated analytically [43] and found to be $N_{11} = 0.0131$, $N_{22} = 0.0336$, and $N_{33} = 0.9533$ (in our case $N_{12} = N_{13} = N_{23} = 0$). Other FL parameters and the conductance of the junction with a typical MgO thickness $t_b = 1$ nm are listed in Table I. Note that the magnetic anisotropy associated with the $\text{Co}_{20}\text{Fe}_{60}\text{B}_{20}$ –overlayer interface [49] is neglected in comparison with that of the $\text{Co}_{20}\text{Fe}_{60}\text{B}_{20}$ –MgO one, and the IEC energy is evaluated via the relation $U_{\text{IEC}} \approx 5.78 \exp(-7.43 \times 10^9 \text{ m}^{-1} t_b) \text{ mJ m}^{-2}$ [48].

The magnetization dynamics is first quantified for the $\text{Co}_{20}\text{Fe}_{60}\text{B}_{20}$ FL covered by the Au layer with the thickness $t_{\text{Au}} = 200$ nm. The voltage drop across the Au overlayer is neglected, because its resistance is much smaller than the MTJ resistance. The displacement current $I_C = CdV_{\text{ac}}/dt$ proportional to the junction's capacitance $C = \varepsilon_0 \varepsilon_{\text{MgO}} A / t_b$ (A is the MTJ area, $\varepsilon_{\text{MgO}} = 9.8$ is the barrier permittivity [50]) is found to be insignificant in comparison with the tunnel current $I_{\text{tun}} \geq G_{\text{AP}} V_{\text{ac}}$, because the ratio $2\pi f C / (G_{\text{AP}} A)$ is less than 10% even at the highest studied frequency $v = 1.7$ GHz. Since gold is a good heat conductor, we also ignore the FL heating caused by the microwave current, which leads to significant heat-driven spin torques in the $\text{Co}_{20}\text{Fe}_{60}\text{B}_{20}$ /MgO/Fe-B/MgO heterostructure [51].

To evaluate the reflection spin-mixing conductance $g_{\uparrow\downarrow}^r$ of the $\text{Co}_{20}\text{Fe}_{60}\text{B}_{20}$ –Au interface, we use the theoretical estimate obtained for the Fe–Au one [38]. Taking $\text{Re}[g_{\uparrow\downarrow}^r] = 1.2 \times 10^{19} \text{ m}^{-2}$, from Eq. (2) we obtain $\alpha = 0.019$ for the renormalized damping parameter. Since $\text{Im}[g_{\uparrow\downarrow}^r]$ should be negligible at the considered FL thickness $t_{\text{FL}} = 1.69$ nm, which is well above a few-monolayer range, the parameter γ is set equal to γ_0 . It should be noted that the spin backflow into FL caused by the spin accumulation in the overlayer reduces the renormalized damping parameter α [52]. However, this reduction increases the amplitude of magnetization oscillations and may be ignored in the first approximation at the

considered thickness $t_{\text{Au}} = 200$ nm, which is much larger than the spin diffusion length $\lambda_{\text{SD}} = 35$ nm in Au [12].

The numerical calculations are focused on the determination of the frequency dependence of magnetization precession at different amplitudes V_{max} of the applied microwave voltage. As a suitable characteristic of the precession magnitude, we employ the sweep $\Delta m_1 = m_1^{\text{max}} - m_1^{\text{min}}$ of the scalar product $\mathbf{m} \cdot \mathbf{m}_{\text{RL}}$ that governs the MTJ conductance $G = G_P(1 + \eta^2 \mathbf{m} \cdot \mathbf{m}_{\text{RL}})/(1 + \eta^2)$. It is found that, at small voltages $V_{\text{max}} \leq 20$ mV, the dependence $\Delta m_1(f)$ involves a strong symmetric peak situated at the resonance frequency $f_{\text{res}} \simeq 1.33$ GHz and a finite number of minute peaks located at frequencies $f_n = f_{\text{res}}/n$ ($n = 2, 3, 4, \dots$). As the voltage V_{max} increases, all peaks grow, gradually become asymmetric, and shift to lower frequencies $f_{\text{res}}(V_{\text{max}})$ and $f_n(V_{\text{max}}) \neq f_{\text{res}}(V_{\text{max}})/n$ [see Fig. 2(a)]. Remarkably, the steep segment of $\Delta m_1(f)$ just below the frequency f_{res} of the main peak breaks above a threshold amplitude $V_{\text{max}} = V_{\text{th}} \approx 205$ mV [see Fig. 2(b)]. When V_{max} increases up to about 600 mV, similar breaks appear at the frequencies f_n of the secondary peaks and a second break of the main peak emerges at $f > f_{\text{res}}$ [Fig. 2(c)].

Peculiar dependences of the precession amplitude on the frequency of applied voltage, which appear at $V_{\text{max}} > V_{\text{th}}$, are solely due to nonlinearity of the function $\Delta F(\mathbf{m})$ defined by Eq. (3). Indeed, when only the STT and some fixed effective field \mathbf{H}_{eff} are taken into account in the numerical calculations, the dependence $\Delta m_1(f)$ assumes the standard form with a single symmetric peak situated at corresponding resonance frequency. Furthermore, the distorted shape of the main peak and the hysteresis shown in Fig. 2(b) can be explained by considering the effective field \mathbf{H}_{eff} involved in Eq. (1). In the first approximation, the

out-of-plane component of \mathbf{H}_{eff} can be written as

$$H_3^{\text{eff}} = - \left(\frac{2K_s}{\mu_0 M_s t_{\text{FL}}} + M_s N_{33} \right) m_3, \quad (4)$$

where the sum in the brackets is negative owing to the prevailing perpendicular anisotropy created by the $\text{Co}_{20}\text{Fe}_{60}\text{B}_{20}$ –MgO interface. If the excitation frequency approaches f_{res} from below, the precession sweep $\Delta m_1(f)$ increases, which reduces the average direction cosine $\langle m_3 \rangle$ of the precessing magnetization. Hence according to Eq. (4) the average effective field $\langle H_3^{\text{eff}} \rangle$ decreases, leading to a reduction in the resonance frequency f_{res} of the large-angle precession. As a result, the precession amplitude increases further and further and eventually jumps to the right branch of the resonance curve at some frequency f_{up} . On the other hand, when the excitation frequency decreases towards f_{res} from above, the accompanying increase of $\Delta m_1(f)$ and reduction of $\langle m_3 \rangle$ lower the resonance frequency. This effect extends the right branch of the resonance curve to frequencies below f_{up} , but the precession amplitude drops down to the left branch at some frequency $f_{\text{down}} < f_{\text{up}}$, because small decrease of f_{res} does not compensate further reduction of f . The above considerations explain the hysteresis of $\Delta m_1(f)$ and the position of the break on the frequency scale.

The distortion of the main peak, which we reveal for the large-angle magnetization precession in the ultrathin $\text{Co}_{20}\text{Fe}_{60}\text{B}_{20}$ layer with perpendicular anisotropy, corresponds to the behavior of a Duffing oscillator with a softening nonlinearity [53]. A similar “foldover” effect is observed for the STT-driven magnetization dynamics in the Co/Ni multilayer excited by a microwave current [54]. However, such a multilayer represents a hardening

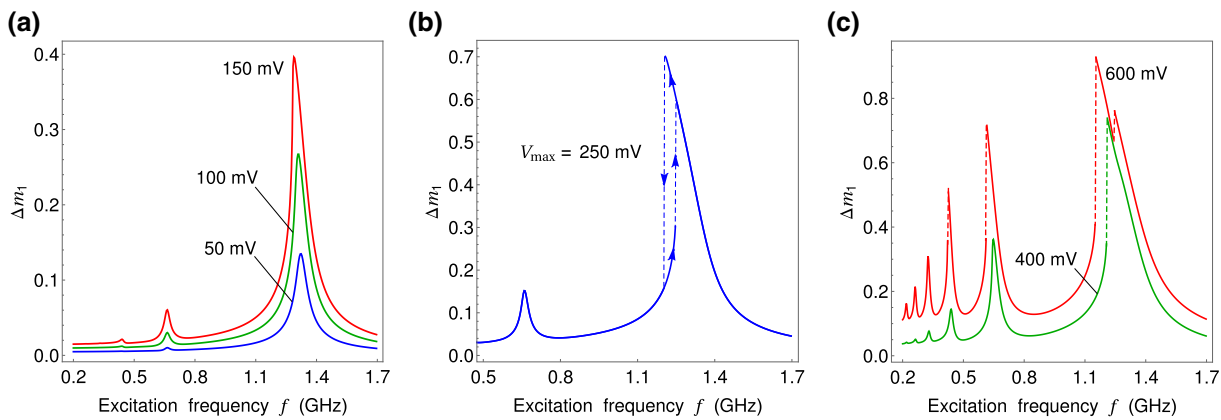


FIG. 2. Frequency dependences of the amplitude of magnetization precession in the free $\text{Co}_{20}\text{Fe}_{60}\text{B}_{20}$ layer covered by Au calculated at different amplitudes V_{max} of the microwave voltage applied to the tunnel junction. Each new simulation starts from a steady-state precession generated during the previous simulation performed at a slightly differing excitation frequency. The graphs show the swing Δm_1 of the scalar product $\mathbf{m} \cdot \mathbf{m}_{\text{RL}}$ of the unit vectors directed along the FL and RL magnetizations. Voltage amplitudes V_{max} are indicated near the curves. Panels (a), (b) present $\Delta m_1(f)$ calculated at both increasing and decreasing voltage frequency f , whereas panel (c) shows results only for increasing frequency.

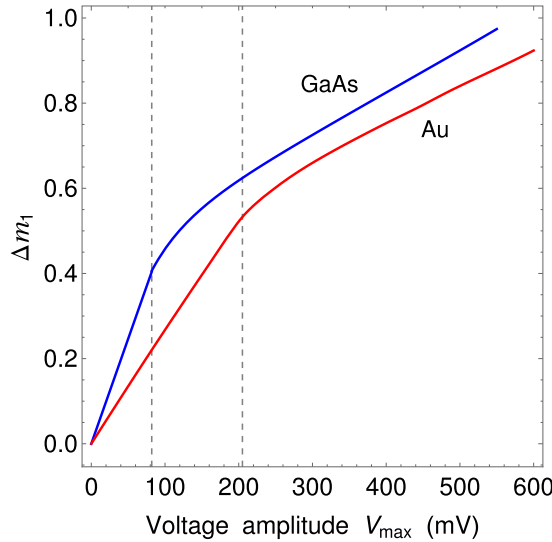


FIG. 3. Height $\Delta m_1(f_{\text{res}})$ of the main peak in the frequency dependence of magnetization precession plotted as a function of the amplitude V_{max} of applied microwave voltage. Red and blue curves show results obtained for the free $\text{Co}_{20}\text{Fe}_{60}\text{B}_{20}$ layer covered by Au and GaAs, respectively. Vertical dashed lines indicate the threshold voltage V_{th} .

system due to the condition $H_3^{\text{eff}}/m_3 < 0$ caused by the prevailing shape anisotropy. Therefore, the resonance curve should have a break on its right branch when plotted on the frequency scale, which is supported by the experimental results [54] and theoretical calculations [55]. It should be noted that the “foldover” effect is absent in the case of magnetization precession induced by a microwave current in an in-plane magnetized ferromagnetic film subjected to in-plane magnetic field [55]. Our model explains this feature by a small time-averaged value of the direction cosine m_3 , which is characteristic of such a precession. Indeed, according to Eq. (4) the mean value of the effective field component H_3^{eff} does not change significantly with increasing precession amplitude, while the components H_1^{eff} and H_2^{eff} are negligible due to small demagnetizing factors N_{11} and N_{22} . Hence, the mean effective field $\langle \mathbf{H}_{\text{eff}} \rangle$ remains to be almost constant, and the “foldover” effect does not appear.

Figure 3 shows the height $\Delta m_1(f_{\text{res}})$ of the main peak appearing at increasing frequency f as a function of the voltage amplitude V_{max} . At $V_{\text{max}} < V_{\text{th}}$, the peak height varies linearly with V_{max} , but at higher voltages the variation of $\Delta m_1(f_{\text{res}})$ becomes nonlinear, which is in line with the significant change of the frequency dependence $\Delta m_1(f)$ appearing above V_{th} . Remarkably, $\Delta m_1(f_{\text{res}})$ continues to increase with voltage even near $V_{\text{max}} = 600$ mV, which is due to strong STT acting on the FL magnetization at the considered small barrier thickness $t_b = 1$ nm. The revealed behavior is different from the voltage dependence of the precession amplitude in the

$\text{Co}_{20}\text{Fe}_{60}\text{B}_{20}/\text{MgO}/\text{Co}_{20}\text{Fe}_{60}\text{B}_{20}$ junction with the MgO thickness of 2 nm [56], which saturates at $V_{\text{max}} \sim 300$ mV due to negligible STT at such t_b . It should be noted that, in the range of small voltages $V_{\text{max}} \ll V_{\text{th}}$, the results of our numerical calculations agree with those obtained analytically by solving the linearized LLGS equation. This agreement confirms the validity of our computations.

To clarify the origin of the secondary peaks, we determine the trajectories of the end of the unit vector \mathbf{m} during the magnetization oscillations generated at different excitation frequencies for a representative voltage amplitude $V_{\text{max}} = 400$ mV. Figure 4 shows projections of these trajectories on the (x_1, x_2) plane, which arise at the frequencies f_{res} and $f_n (n = 2, 3)$ corresponding to the peaks of $\Delta m_1(f)$, in comparison with those formed at frequencies between f_{res}, f_2 , and f_3 . It can be seen that, at $f = f_n$, the magnetization makes n full turns around the equilibrium direction during one period $1/f_n$ of the voltage oscillation. Since $f_n \approx f_{\text{res}}/n$, the mean period of the forced magnetization precession appears to be close to the period $1/f_{\text{res}}$ of free oscillations, which explains enhancement of the precession amplitude at frequencies f_n . Evidently, the above condition cannot be fulfilled at excitation frequencies significantly differing from f_{res}/n . It should be noted that the predicted secondary peaks are an attribute of parametric resonance [57], which occurs when the natural oscillation frequency is varied by an external stimulus. Owing to VCMA, the application of microwave voltage modifies the absolute value $|\mathbf{H}_{\text{eff}}|$ of the effective field, which governs the natural precession frequency. Therefore, the presence of VCMA is responsible for the revealed secondary peaks. It should be noted that VCMA increases the height of the main peak as well. Supplementary calculations show that, at low applied voltages $V_{\text{max}} < 20$ mV, the height of this peak reduces by about 2 times when the voltage dependence of the interfacial magnetic anisotropy is ignored. This result shows that at such V_{max} the torque created by VCMA is comparable to the STT. However, as the voltage V_{max} increases, the relative role of VCMA decreases due to the reduction of the mean value of the direction cosine m_3 , and the growth of the main peak at high voltages $V_{\text{max}} > 200$ mV is almost solely due to the increase of STT.

Similar frequency and voltage dependences are obtained for the electrically driven magnetization precession in the $\text{Co}_{20}\text{Fe}_{60}\text{B}_{20}$ free layer covered by GaAs. Since the reflection spin-mixing conductance $g_{\uparrow\downarrow}^r$ of the $\text{Co}_{20}\text{Fe}_{60}\text{B}_{20}$ –GaAs interface is expected to be relatively small in comparison with that of the $\text{Co}_{20}\text{Fe}_{60}\text{B}_{20}$ –Au one [15], the influence of the spin pumping on the parameters γ and α involved in Eq. (1) can be ignored. Therefore, the magnetic damping becomes smaller ($\alpha = 0.01$), which leads to higher peaks of $\Delta m_1(f)$ in the free layer covered by GaAs. The voltage dependence of the height $\Delta m_1(f_{\text{res}})$ of the main peak appearing at increasing the excitation

frequency is shown in Fig. 3. It is qualitatively similar to the voltage dependence obtained for the $\text{Co}_{20}\text{Fe}_{60}\text{B}_{20}$ free layer covered by Au, but differs by larger values of $\Delta m_1(f_{\text{res}})$ and a smaller threshold voltage $V_{\text{th}} \approx 82$ mV.

In conclusion of this section we note that the magnetization dynamics generated by a microwave voltage is very different from that excited by a direct current flowing through the MTJ [58]. Indeed, the microwave voltage induces a forced magnetization precession governed by the excitation frequency, whereas the direct current gives rise to magnetization auto-oscillations with a frequency depending on the current density. As a result, the precession amplitude has a peculiar frequency dependence with a sharp main peak and smaller secondary peaks (Fig. 2). In contrast, the frequency of auto-oscillations exhibits only a limited variation in the “precession window,” while their amplitude as a function of the current density has a broad maximum [58].

III. SPIN INJECTION AND PUMPING INTO METALLIC OVERLAYER

Using the results obtained for the magnetization dynamics induced by the microwave voltage applied to the $\text{Co}_{20}\text{Fe}_{60}\text{B}_{20}/\text{MgO}/\text{Co}_{20}\text{Fe}_{60}\text{B}_{20}$ junction, we calculate the spin current generated in the Au overlayer near the interface with FL. In our case, such a current is the sum of two contributions, which result from the spin pumping caused by the magnetization precession and the spin injection proportional to the spin polarization of the charge

TABLE I. Parameters of the $\text{Co}_{20}\text{Fe}_{60}\text{B}_{20}$ free layer and the $\text{Co}_{20}\text{Fe}_{60}\text{B}_{20}/\text{MgO}/\text{Co}_{20}\text{Fe}_{60}\text{B}_{20}$ tunnel junction used in numerical calculations.

Parameter	Value	Reference
M_s	$1.13 \times 10^6 \text{ A m}^{-1}$	[44]
α_0	0.01	[34]
K_1	5 kJ m^{-3}	[45]
K_s^0	$-1.3 \times 10^{-3} \text{ J m}^{-2}$	[34]
k_s	$31 \text{ fJ V}^{-1} \text{ m}^{-1}$	[41]
G_P	$1.778 \times 10^{10} \text{ S m}^{-2}$	[46]
η	0.577	[34]
p_{FL}	0.53	[47]
U_{IEC}	$3.4 \mu\text{J m}^{-2}$	[48]

current. Since the spin current is characterized by the direction of spin flow and the orientation of spin polarization, we employ a second-rank tensor \mathbf{J}_s to define the spin-current density [59]. At the considered FL thickness, the pumped spin-current density \mathbf{J}_{SP} near the $\text{Co}_{20}\text{Fe}_{60}\text{B}_{20}$ -Au interface can be evaluated using the formula $\mathbf{e}_n \cdot \mathbf{J}_{\text{SP}} \simeq (\hbar/4\pi)\text{Re}[g_{\uparrow\downarrow}^r]\mathbf{m} \times d\mathbf{m}/dt$, where \mathbf{e}_n is the unit normal vector to the interface pointing into Au, and $\text{Re}[g_{\uparrow\downarrow}^r]$ may be set equal to $1.2 \times 10^{19} \text{ m}^{-2}$ [38]. The spin injection created by the charge current with the density $J_c = GV_{\text{ac}}$ is described by the relation

$$\mathbf{e}_n \cdot \mathbf{J}_{\text{SI}} \simeq -\frac{\hbar}{2e} G_P \frac{1 + \eta^2 \mathbf{m} \cdot \mathbf{m}_{\text{RL}}}{1 + \eta^2} V_{\text{ac}} p_{\text{FL}} \mathbf{m}, \quad (5)$$

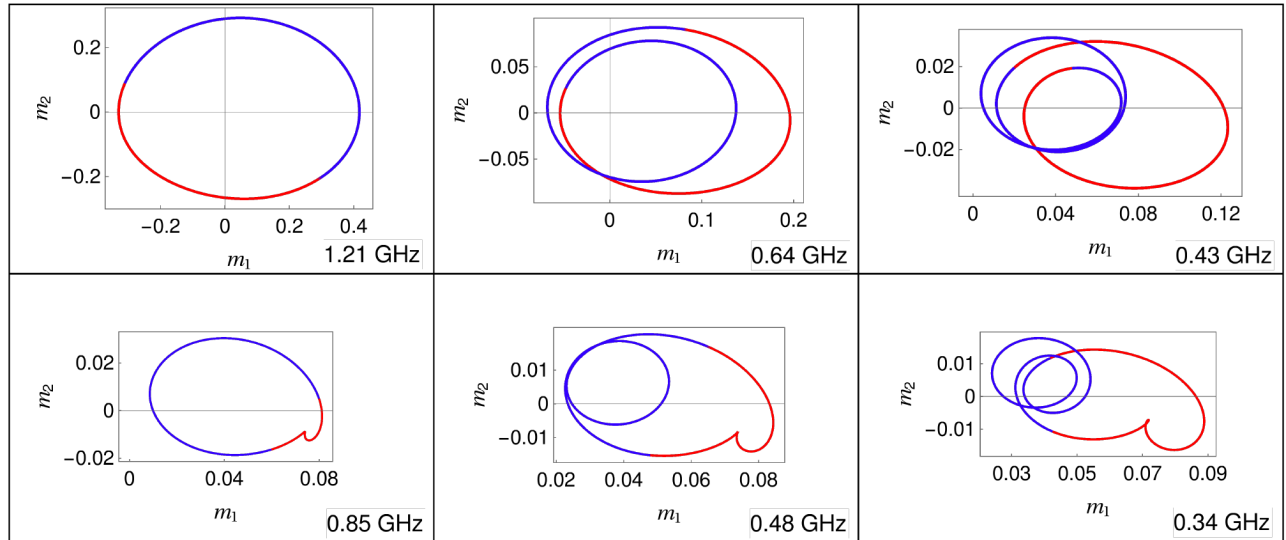


FIG. 4. Trajectories of the end of the unit vector \mathbf{m} during the magnetization precession in the free $\text{Co}_{20}\text{Fe}_{60}\text{B}_{20}$ layer covered by Au. Curves show projections of these trajectories on the (x_1, x_2) plane parallel to the $\text{Co}_{20}\text{Fe}_{60}\text{B}_{20}$ surfaces. Trajectories are calculated at different frequencies f of the applied microwave voltage V_{ac} with the amplitude $V_{\text{max}} = 400$ mV, which are indicated in the figure. The upper row shows trajectories arising at the excitation frequencies f_{res} and $f_n(n = 2, 3)$ corresponding to the peaks of $\Delta m_1(f)$, whereas the lower row presents those forming at frequencies between f_{res}, f_2 , and f_3 . Positive and negative values of the applied voltage $V_{\text{ac}}(t)$ are indicated by red and blue color, respectively.

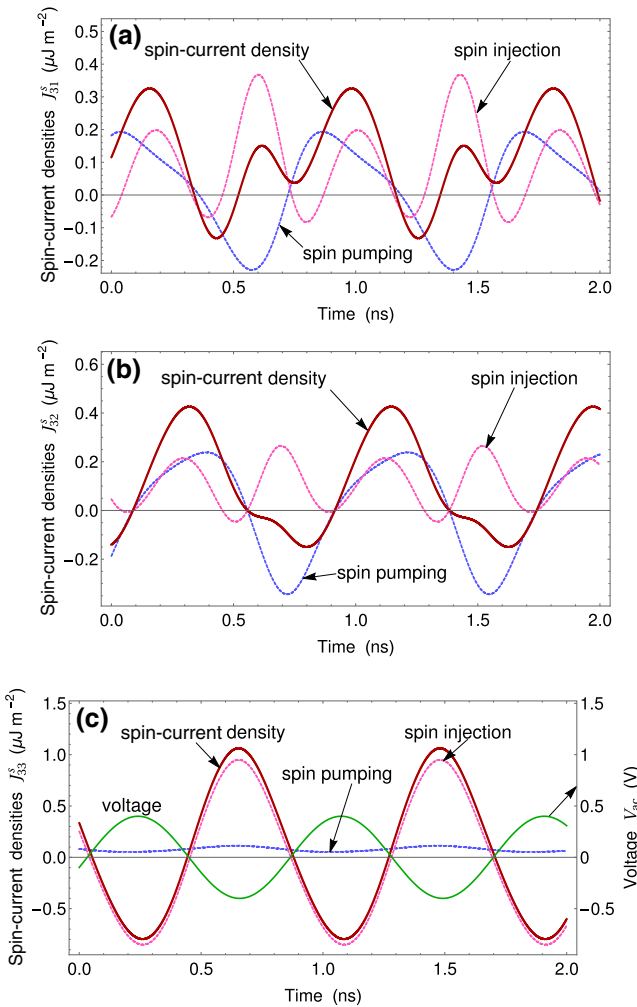


FIG. 5. Time dependences of the total spin-current densities J_{31}^s (a), J_{32}^s (b), and J_{33}^s (c) generated at the Au–Co₂₀Fe₆₀B₂₀ interface by the microwave voltage with the frequency $f_{res} = 1.2$ GHz and amplitude $V_{max} = 400$ mV. Contributions of spin-polarized charge current and precession-induced spin pumping are shown by pink and blue lines, respectively.

where $p_{FL} = (N_\uparrow - N_\downarrow)/(N_\uparrow + N_\downarrow)$ is the spin polarization in the FL having the densities of states N_\uparrow and N_\downarrow of spin-up and spin-down electrons at the Fermi level, respectively. It should be noted that the spin flow along the Co₂₀Fe₆₀B₂₀–Au interface, which is caused by the spin Hall effect, has a negligible magnitude in comparison with that of the spin flow in the direction orthogonal to the interface.

Representative results obtained for variations of the total spin-current density $\mathbf{J}_s = \mathbf{J}_{SP} + \mathbf{J}_{SI}$ with time are presented in Fig. 5. Since the discussed spin current flows along the x_3 axis of our coordinate system shown in Fig. 1, the only nonzero elements of the tensor \mathbf{J}_s are J_{3k}^s ($k = 1, 2, 3$). Figure 5 shows that, at the considered high voltage amplitude $V_{max} = 400$ mV, $J_{31}^s(t)$ and $J_{32}^s(t)$ exhibit strongly

TABLE II. Ac and dc components of spin-current densities plotted in Fig. 5. Numerical values are given in units of $\mu\text{J m}^{-2}$.

i	ac components			dc components		
	J_{3i}^{SP}	J_{3i}^{SI}	J_{3i}^s	J_{3i}^{SP}	J_{3i}^{SI}	J_{3i}^s
1	0.42	0.45	0.46	0.02	0.10	0.12
2	0.58	0.31	0.58	0.02	0.10	0.12
3	0.06	1.80	1.86	0.08	-0.07	0.01

nonsinusoidal time dependences, whereas $J_{33}^s(t)$ is distinguished by an approximately sinusoidal one. Concerning the contributions of precession-induced spin pumping and spin-polarized charge current, we see that the sweep of $J_{31}^{SP}(t)$ is almost the same as the $J_{31}^{SI}(t)$ one, while the sweep of $J_{32}^{SP}(t)$ is noticeably bigger than that of $J_{32}^{SI}(t)$. In contrast, the sweep of $J_{33}^{SI}(t)$ is much larger than that of the density $J_{33}^{SP}(t)$, which does not change sign and varies with time only slightly (Fig. 5).

The sweep ΔJ_{3k}^s characterizes the ac component of the spin-current density $J_{3k}^s(t)$, and the dc component $\langle J_{3k}^s \rangle$ can be determined by averaging $J_{3k}^s(t)$ over the period $1/f$ of voltage oscillations. Note that $J_{31}^{SI}(t)$ and $J_{32}^{SI}(t)$ oscillate with the double excitation frequency $2f$, because the magnetization projections $m_1(t)$ and $m_2(t)$ involved in Eq. (5) undergo significant variations with time (see Fig. 4). Interestingly, the numerical calculations show that the spin injection $J_{32}^{SI}(t)$ does not significantly influence the ac component of the total spin-current density $J_{32}^s(t)$. Therefore, the ac component of $J_{32}^s(t)$ practically equals that of $J_{32}^{SP}(t)$, thus characterizing the precession-induced spin current. Furthermore, the dc component of $J_{32}^{SP}(t)$ is almost zero so that the time-averaged value of $J_{32}^s(t)$ is governed by the spin injection. Numerical values of the ac and dc components of the spin-current densities plotted in Fig. 5 are given in Table II. It should be noted that the ac component of the total spin-current density usually differs from the sum of the ac components of the spin pumping and spin injection, which is due to the phase shifts between their oscillations clearly seen in Fig. 5.

Figure 6 shows variations of the ac components ΔJ_{31}^s , ΔJ_{32}^s , and ΔJ_{33}^s with the excitation frequency f , which take place near the resonance frequency f_{res} of the magnetization precession. It can be seen that ΔJ_{31}^s and ΔJ_{32}^s have a strong peak at f_{res} , while ΔJ_{33}^s only weakly depends on the excitation frequency. Remarkably, the secondary peak of ΔJ_{31}^s and ΔJ_{32}^s , which is located at $f \approx f_{res}/2$, rapidly grows with increasing voltage amplitude V_{max} and becomes comparable in magnitude with the main peak at $V_{max} \geq 400$ mV. In contrast, the dc spin-current densities $\langle J_{3k}^s \rangle$ exhibit strong peaks near f_{res} only (see Fig. 7). To illustrate the influence of the voltage amplitude V_{max} on the spin-current density generated near the Co₂₀Fe₆₀B₂₀–Au interface, we present in Fig. 8 the dependences $\Delta J_{32}^s(V_{max})$ and $\langle J_{32}^s \rangle(V_{max})$ evaluated at the

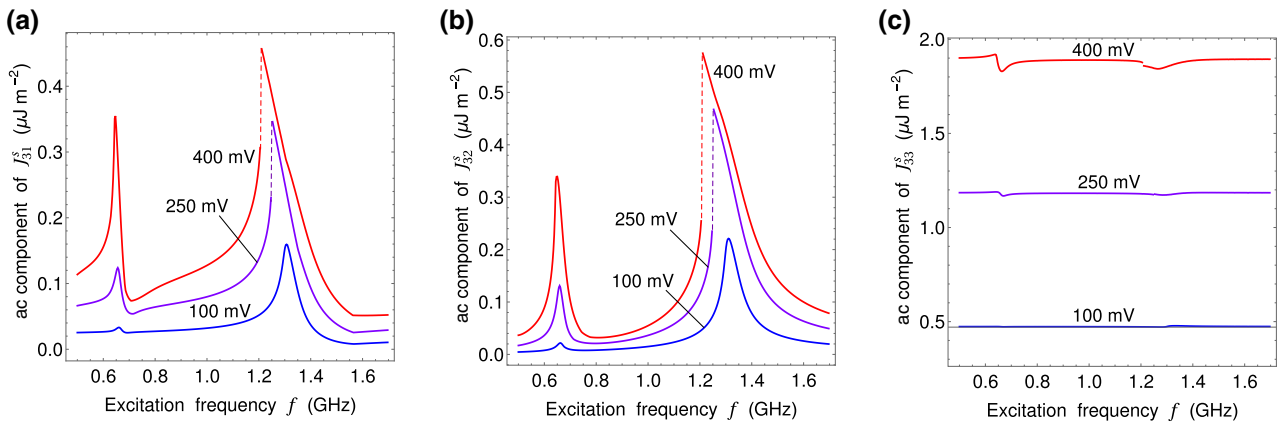


FIG. 6. Frequency dependences of the ac components of spin-current densities J_{31}^s (a), J_{32}^s (b), and J_{33}^s (c) generated at the Au–Co₂₀Fe₆₀B₂₀ interface by microwave voltages with different amplitudes V_{\max} indicated near the graphs.

voltage-dependent resonance frequency $f_{\text{res}}(V_{\max})$. Below the threshold amplitude $V_{\text{th}} \approx 205$ mV, the ac component varies with V_{\max} almost linearly, whereas the dc component follows the power law $\langle J_{32}^s \rangle \propto V_{\max}^2$. At higher voltage amplitudes, both ΔJ_{32}^s and $\langle J_{32}^s \rangle$ increase slower than expected from the above dependences, but at $V_{\max} = 600$ mV they reach significantly enhanced values of about 0.7 and 0.2 $\mu\text{J m}^{-2}$, respectively. It should be emphasized that these values differ strongly from the spin-current densities $\Delta J_{32}^s \sim 0.1 \mu\text{J m}^{-2}$ and $\langle J_{32}^s \rangle \sim 2 \mu\text{J m}^{-2}$ generated by the Co₂₀Fe₆₀B₂₀/MgO/Co₂₀Fe₆₀B₂₀ MTJ excited by direct charge current [58]. Hence the proposed “ac injector” generates the ac spin current much more efficiently than the “dc injector” described in our previous paper [58], while the dc injector is superior for the creation of the dc spin current in normal metals. It is worth noting that the ac injector also has a better tunability than the dc injector. Indeed, the operation frequency of a particular dc injector can be tuned over a limited range only, whereas the ac injector can function in a wider range of microwave frequencies differing by several times and provides the frequency multiplication.

Furthermore, the spin-current density generated by the ac injector can be changed drastically by varying the excitation frequency and amplitude (Figs. 6 and 7), while the spin-current density created by the dc injector varies by less than 2 times in the precession window [58].

The spin-current densities J_{3k}^s presented in Figs. 5–8 are partially suppressed at the interface by the spin backflow \mathbf{J}_{SB} . The product $\mathbf{e}_n \cdot \mathbf{J}_{\text{SB}}$ consists of the components parallel and perpendicular to the magnetization direction \mathbf{m} , which are caused by spin injection and spin pumping, respectively [see Eq. (5) and expression for spin pumping]. Numerical estimates show that the conductance mismatch problem does not appear for the Co₂₀Fe₆₀B₂₀–Au interface. Accordingly, the longitudinal spin backflow is negligible compared to \mathbf{J}_{SI} in our case. In contrast, the transverse spin backflow reduces the spin pumping significantly. To calculate the actual spin-current density $\mathbf{J}_{\text{Au}}(x_3)$ in Au, we solve the spin diffusion equation with appropriate boundary conditions for spin injection and pumping. The boundary condition at $x_3 = t_{\text{Au}}$ represents zero spin flux. The boundary condition at the interface reads $\mathbf{e}_n \cdot$

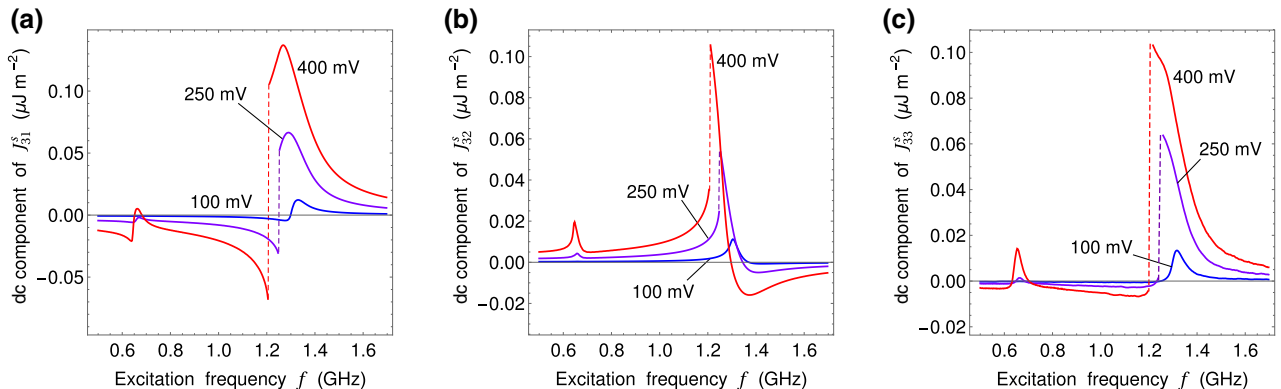


FIG. 7. Frequency dependences of the dc components of spin-current densities J_{31}^s (a), J_{32}^s (b), and J_{33}^s (c) generated at the Au–Co₂₀Fe₆₀B₂₀ interface by microwave voltages with different amplitudes V_{\max} indicated near the graphs.

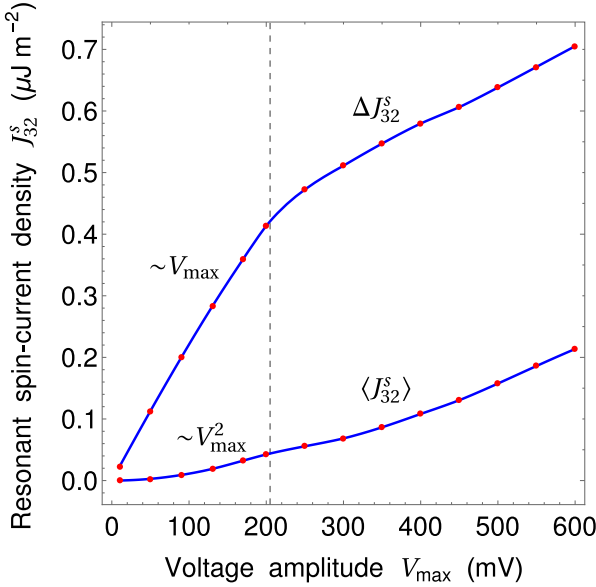


FIG. 8. Dependences of the ac and dc components ΔJ_{32}^s and $\langle J_{32}^s \rangle$ of the spin-current density J_{32}^s on the voltage amplitude V_{\max} , which are evaluated at the voltage-dependent resonance frequency $f_{\text{res}}(V_{\max})$. Vertical dashed line indicates the threshold voltage amplitude V_{th} .

$\mathbf{J}_{\text{Au}} = \mathbf{e}_n \cdot \mathbf{J}_{\text{SI}} + \mathbf{e}_n \cdot \mathbf{J}_{\text{SP}} - \text{Re}[g_{\uparrow\downarrow}^r] \boldsymbol{\mu}_s / 4\pi$ [8], where $\boldsymbol{\mu}_s$ is the spin accumulation in Au near the interface. It should be noted that in our case $\boldsymbol{\mu}_s = 2k_B T(N_{\uparrow} - N_{\downarrow})/(N_{\uparrow} + N_{\downarrow})$, where N_{\uparrow} and N_{\downarrow} are the densities of states in Au, which characterize spin-up and spin-down electrons at the Fermi level. The introduction of spin accumulation allows us to express the diffusive spin-current density in Au as $\mathbf{J}_{\text{Au}} = -[\sigma_{\text{Au}} \hbar / (4e^2)] \partial \boldsymbol{\mu}_s / \partial \mathbf{r}$ [60], where σ_{Au} is the electrical conductivity of Au. Solving the diffusion equation in the adiabatic approximation [60], we obtain an analytic relation

$$\mathbf{J}_{\text{Au}}(x_3) = \frac{\sinh[(t_{\text{Au}} - x_3)/\lambda_{\text{SD}}]}{\sinh[t_{\text{Au}}/\lambda_{\text{SD}}]} \left\{ \mathbf{J}_{\text{SI}} + \mathbf{J}_{\text{SP}} \left(1 + \text{Re}[g_{\uparrow\downarrow}^r] \frac{\lambda_{\text{SD}} e^2}{\pi \sigma_{\text{Au}} \hbar} \coth \frac{t_{\text{Au}}}{\lambda_{\text{SD}}} \right)^{-1} \right\}, \quad (6)$$

which describes how \mathbf{J}_{Au} decays with the distance x_3 from the $\text{Co}_{20}\text{Fe}_{60}\text{B}_{20}$ –Au interface due to spin relaxation and diffusion. Equation (6) is similar to the formula presented in Ref. [12], but differs by the spin-current density at the interface $\mathbf{J}_{\text{SI}} + \mathbf{J}_{\text{SP}}\beta$, where β is the backflow factor. Taking $\sigma_{\text{Au}} = 4.5 \times 10^7 \text{ S m}^{-1}$ [61], we find $\beta \approx 0.6$ so that the actual spin pumping into Au is smaller than \mathbf{J}_{SP} by about 40%.

Our theoretical results demonstrate that the $\text{Co}_{20}\text{Fe}_{60}\text{B}_{20}$ – $\text{MgO}/\text{Co}_{20}\text{Fe}_{60}\text{B}_{20}$ tunnel junction subjected to a microwave

voltage with an appropriate frequency represents a promising spin injector into normal metals. Since the generated spin current creates a charge current owing to the inverse spin Hall effect (ISHE), the efficiency of spin injection can be probed electrically [11]. Motivated by this opportunity, we calculate distributions of the charge-current density $\mathbf{J}_c(\mathbf{r}, t)$ and electric potential $\phi(\mathbf{r}, t)$ in the Au overlayer in the quasistatic approximation [58]. As the ISHE contribution \mathbf{J}_{ISHE} to the density \mathbf{J}_c is governed by the vector product of the spin accumulation $\boldsymbol{\mu}_s$ and the unit vector \mathbf{e}_s directed along the spin flow [62], the element J_{33}^{Au} of the spin-current-density tensor \mathbf{J}_{Au} does not affect \mathbf{J}_{ISHE} and can be disregarded. Further, the elements J_{31}^{Au} and J_{32}^{Au} create contributions only to the projections of \mathbf{J}_{ISHE} on the orthogonal axes x_2 and x_1 , respectively. Restricting our calculations to the determination of the charge transport in the (x_1, x_3) plane, which governs the transverse voltage $V_1(x_3) = \phi(x_1 = L_1, x_3) - \phi(x_1 = 0, x_3)$ between the sides of Au overlayer normal to the x_1 axis (Fig. 1), we may disregard J_{31}^{Au} as well. For the relevant projection J_1^{ISHE} of the ISHE current density, the theory gives $J_1^{\text{ISHE}}(x_1) = \alpha_{\text{SH}}(2e/\hbar) J_{32}^{\text{Au}}(x_3)$, where $\alpha_{\text{SH}} = 0.0035$ is the spin Hall angle of Au [12], and the spin-current density J_{32}^{Au} is determined by Eq. (6).

The total density \mathbf{J}_c of the charge current flowing in the Au layer is the sum of the ISHE contribution \mathbf{J}_{ISHE} and the drift contribution $\mathbf{J}_{\text{drift}} = -\sigma_{\text{Au}} \nabla \phi$. To calculate the electric potential $\phi(\mathbf{r}, t)$, we use Laplace's equation $\nabla^2 \phi = 0$ appended by appropriate boundary conditions. Namely, the charge-current density J_3^c at the $\text{Co}_{20}\text{Fe}_{60}\text{B}_{20}$ –Au interface $x_3 = 0$ is set equal to the density $J_c = GV_{\text{ac}}$ of the tunnel current, which is assumed uniform, because the anomalous Hall effect in the $\text{Co}_{20}\text{Fe}_{60}\text{B}_{20}$ layer has a weak effect on the transverse voltage $V_1(x_3)$ [58]. The same boundary condition is introduced at the upper boundary $x_3 = t_{\text{Au}}$ of the Au overlayer to exclude the charge accumulation in Au. At the side boundaries $x_1 = 0$ and $x_1 = L_1$ of the overlayer, the total current density J_3^c should go to zero, which yields $\sigma_{\text{Au}} \partial \phi / \partial x_1 = J_1^{\text{ISHE}}$, where J_1^{ISHE} is directly proportional to the spin-current density given by Eq. (6). Remarkably, because of this condition the transverse voltage $V_1(x_3, t)$ at any time moment is a linear combination of $J_{32}^{\text{SP}}(t)$ and $J_{32}^{\text{SI}}(t)$ presented in Fig. 5. Taking into account that $\Delta(J_{32}^{\text{SI}} + J_{32}^{\text{SP}}) \approx \Delta J_{32}^{\text{SP}}$ and $\langle J_{32}^{\text{SI}} + J_{32}^{\text{SP}} \rangle \approx \langle J_{32}^{\text{SI}} \rangle$, we find that the ac component $\Delta V_1(x_3)$ of the transverse voltage is proportional to spin pumping, whereas the dc component $\langle V_1 \rangle(x_3)$ is proportional to spin injection. Hence a certain tunneling heterostructure has the universal dependences of the normalized voltages $\Delta V_1(x_3)/\Delta J_{32}^s$ and $\langle V_1 \rangle(x_3)/\langle J_{32}^s \rangle$ on the distance x_3 from the interface, which do not depend on the amplitude V_{\max} and frequency f of the electrical excitation.

For the considered spin injector, the numerical calculations demonstrate that the variations of $\Delta V_1(x_3)/\Delta J_{32}^s$ and $\langle V_1 \rangle(x_3)/\langle J_{32}^s \rangle$ follow the curves shown in Fig. 9. Thus,

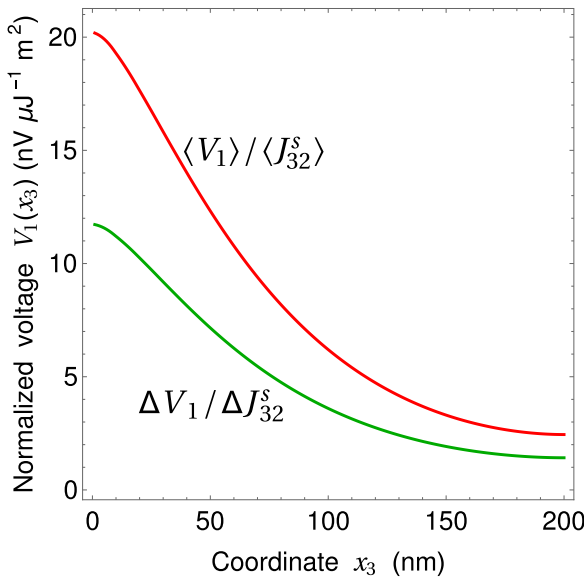


FIG. 9. Normalized transverse voltage between the sides of Au overlayer normal to the x_1 axis plotted as a function of the distance x_3 from the Au–Co₂₀Fe₆₀B₂₀ interface.

using the curves in Fig. 9 together with the data presented in Fig. 8, one can evaluate the voltage swing $\Delta V_1(f_{\text{res}})$ induced by the spin pumping and the time-averaged transverse voltage $\langle V_1 \rangle(f_{\text{res}})$ proportional to the spin injection. At $V_{\text{max}} = 600$ mV and $f_{\text{res}} = 1.16$ GHz, the calculation yields $\Delta V_1 > 6.3$ nV and $\langle V_1 \rangle > 3.6$ nV for the Au region $x_3 < 30$ nm near the interface. The predicted transverse voltages can be detected experimentally, which indicates significant efficiency of the proposed spin injector.

IV. SPIN PUMPING INTO SEMICONDUCTOR

To demonstrate that MTJs excited by microwave voltages can be employed as efficient spin injectors into semiconductors too, we study the spin accumulation in a long GaAs bar connected to the Co₂₀Fe₆₀B₂₀/MgO/Co₂₀Fe₆₀B₂₀ junction and separated from a normal metal (NM) lead by a thin MgO interlayer (see Fig. 10). The length L_{SC} of the GaAs bar is much larger than the FL size L_1 along the x_1 axis, while its width along the x_2 axis is equal to the FL size L_2 . The considered Si-doped GaAs with the donor concentration $N_D = 10^{18}$ cm⁻³ is a degenerate semiconductor [63], which forms an Ohmic contact with Co₂₀Fe₆₀B₂₀. Indeed, n^+ -GaAs has the electron mobility $\chi_{\text{SC}} = 0.23$ m² V⁻¹ s⁻¹ [64] and the conductivity $\sigma_{\text{SC}} = \chi_{\text{SC}} N_D e = 3.68 \times 10^4$ S m⁻¹, which is only one order of magnitude smaller than the conductivity $\sigma_{\text{FL}} = 4.45 \times 10^5$ S m⁻¹ of Co₂₀Fe₆₀B₂₀ [65]. From the measured spin-flip relaxation time $\tau_{\text{SF}} = 0.9$ ns [66] and the diffusion coefficient $D = 6 \times 10^{-3}$ m² s⁻¹ obtained via the Einstein relation it follows that the spin-diffusion length $\lambda_{\text{SC}} =$

$\sqrt{D\tau_{\text{SF}}}$ in n^+ -GaAs amounts to about 2.32 μm at room temperature. Hence the spin accumulation $\boldsymbol{\mu}_s(\mathbf{r})$, which is the difference between the chemical potentials for spins parallel and antiparallel to the direction determined by the total nonequilibrium spin-imbalance density [8], should be homogeneous in the considered GaAs bar with the nanoscale thickness $t_{\text{SC}} = 30$ nm $\ll \lambda_{\text{SD}}$ along the x_3 axis normal to the Co₂₀Fe₆₀B₂₀–GaAs interface. Assuming $\boldsymbol{\mu}_s(\mathbf{r})$ to be uniform along the x_2 axis as well, we obtain a one-dimensional diffusion equation (k_B is the Boltzmann constant)

$$\frac{\partial \boldsymbol{\mu}_s}{\partial t} = \frac{4k_B T}{\hbar N_D t_{\text{SC}}} \mathbf{e}_n \cdot \mathbf{J}_{\Sigma} + D \frac{\partial^2 \boldsymbol{\mu}_s}{\partial x_1^2} - \frac{\boldsymbol{\mu}_s}{\tau_{\text{SF}}} \quad (7)$$

for the sought function $\boldsymbol{\mu}_s(x_1)$. The first term on the rhs of Eq. (7) differs from zero only at $-L_1/2 \leq x_1 \leq L_1/2$ and describes the spin generation in the bar section adjacent to FL. The total spin-current density \mathbf{J}_{Σ} is the sum of four contributions, which result from the spin pumping into GaAs (\mathbf{J}_{SP}), spin injection from FL into GaAs (\mathbf{J}_{SI}), spin backflow from GaAs to FL (\mathbf{J}_{BF}), and spin loss caused by the spin-polarized tunnel current flowing across the MgO interlayer separating GaAs from the NM lead (\mathbf{J}_{SL}). The spin-injection density \mathbf{J}_{SI} can be calculated using Eq. (5), where the FL spin polarization p_{FL} should be replaced by the effective polarization $p_{\text{eff}} = p_{\text{FL}} [1 + (1 - p_{\text{FL}}^2)(\sigma_{\text{FL}} \lambda_{\text{SC}})/(\sigma_{\text{SC}} \lambda_{\text{FL}})]^{-1}$ [5] depending on the Co₂₀Fe₆₀B₂₀ spin-diffusion length $\lambda_{\text{FL}} = 6.2$ nm [67]. With the numerical values of the involved parameters the calculation gives very small effective polarization $p_{\text{eff}} = 1.6 \times 10^{-4}$, which means that the spin injection into n^+ -GaAs is negligible due to small product $\sigma_{\text{SC}} \lambda_{\text{FL}}$ in comparison with $\sigma_{\text{FM}} \lambda_{\text{SC}}$. Accordingly, the spin-accumulation vector $\boldsymbol{\mu}_s$ appears to be almost orthogonal to the FL magnetization \mathbf{M} , and the spin backflow from GaAs to FL can be evaluated via the relation $\mathbf{e}_n \cdot \mathbf{J}_{\text{BF}} \simeq -\text{Re}[g_{\uparrow\downarrow}^r] \boldsymbol{\mu}_s / 4\pi$ [31]. Finally, the spin loss \mathbf{J}_{SL} caused by the charge current J_c flowing across the GaAs–MgO interface equals $\mathbf{e}_n \cdot \mathbf{J}_{\text{SL}} = -(\hbar/2e) J_c \boldsymbol{\mu}_s / (2k_B T)$. The distribution $\boldsymbol{\mu}_s(x_1)$ of spin accumulation along the GaAs bar is calculated by solving Eq. (7) numerically with the boundary condition $\partial \boldsymbol{\mu}_s / \partial x_1 = 0$ at $x_1 = \pm L_{\text{SC}}/2$. We assume that the MgO tunnel barrier separating GaAs from the NM lead has the same conductance G_P as the Co₂₀Fe₆₀B₂₀/MgO/Co₂₀Fe₆₀B₂₀ junction in the state with parallel electrode magnetizations. Since the GaAs resistance is negligible in comparison with that of two MgO barriers, the dependence of the charge current J_c on voltage V applied to the whole heterostructure is approximated by the relation $J_c = V G_P G(m_1) / [G_P + G(m_1)]$. The electrically induced dynamics of the FL magnetization is recalculated with the account of the modified $\tau_{\text{STT}} = (\gamma \hbar/2e)(V_{\text{MTJ}} G_P / t_{\text{FL}}) \eta / (1 + \eta^2)$ and VCMA $K_s = K_s^0 + k_s V_{\text{MTJ}} / t_b$ resulting from a lower voltage

$V_{\text{MTJ}} = V G_P / [G_P + G(m_1)]$ applied to the MTJ. The spin-pumping contribution \mathbf{J}_{SP} to the total spin-current density \mathbf{J}_Σ involved in Eq. (7) is evaluated using the spin-mixing conductance $\text{Re}[g_{\uparrow\downarrow}^r] = 1.5 \times 10^{17} \text{ m}^{-2}$ determined experimentally for the $\text{Ni}_{81}\text{Fe}_{19}$ –GaAs interface [15].

The numerical calculations show that the spin accumulation $\boldsymbol{\mu}_s$ in GaAs is determined by the competition of spin pumping \mathbf{J}_{SP} and spin backflow \mathbf{J}_{BF} across the $\text{Co}_{20}\text{Fe}_{60}\text{B}_{20}$ –GaAs interface, while the spin loss \mathbf{J}_{SL} through the GaAs–MgO interface is negligible in comparison with \mathbf{J}_{BF} . Further, the differences between nonzero

components of \mathbf{J}_{SP} and $\mathbf{J}_{\text{BF}} + \mathbf{J}_{\text{SL}}$ are about 1% only, which shows that near the $\text{Co}_{20}\text{Fe}_{60}\text{B}_{20}$ –GaAs interface the spin accumulation is close to saturation. Taking into account that only \mathbf{J}_{SP} and \mathbf{J}_{BF} create significant contributions to \mathbf{J}_Σ , we solve Eq. (7) analytically. Since the spin-flip relaxation time $\tau_{\text{SF}} = 0.9 \text{ ns}$ is comparable to the period $1/f_{\text{res}} \sim 1 \text{ ns}$ of magnetization precession, the quasistatic approximation cannot be employed, and $\boldsymbol{\mu}_s(x_1)$ should be regarded as a complex quantity. After some mathematical operations, we obtain the following relation between the Fourier components of $\boldsymbol{\mu}_s$ and \mathbf{J}_{SP} :

$$\boldsymbol{\mu}_s^\omega(x_1) = \frac{4k_B T \tau_{\text{SF}}}{\hbar N_D t_{\text{SC}}(1 + i\omega \tau_{\text{SF}})\chi} \mathbf{e}_n \cdot \mathbf{J}_{\text{SP}}^\omega \begin{cases} \frac{1}{\chi} - \frac{\cosh(2x_1\kappa\chi)\text{csch}(L_1\chi\kappa)}{\chi^2 \coth[(L_{\text{SC}} - L_1)\kappa] + \chi \coth(L_1\chi\kappa)}, & |x_1| < \frac{L_1}{2} \\ \frac{\cosh[(L_{\text{SC}} - 2|x_1|)\kappa]\text{csch}[(L_{\text{SC}} - L_1)\kappa]}{\chi \coth[(L_{\text{SC}} - L_1)\kappa] + \coth(L_1\chi\kappa)}, & |x_1| > \frac{L_1}{2}, \end{cases} \quad (8)$$

where $\kappa = \sqrt{1 + i\omega\tau_{\text{SF}}}/(2\lambda_{\text{SC}})$ and $\chi = \sqrt{1 + k_B T \tau_{\text{SF}} \text{Re}[g_{\uparrow\downarrow}^r]/[\pi \hbar N_D t_{\text{SC}}(1 + i\omega \tau_{\text{SF}})]}$. By combining Eq. (8) with numerical results obtained for the electrically driven precession of the FL magnetization $\mathbf{m}(t)$ and the accompanying spin pumping $\mathbf{J}_{\text{SP}}(\mathbf{m})$, one can calculate the spin accumulation $\boldsymbol{\mu}_s$ as a function of the distance $|x_1|$ from the bar center and the time t . At small frequencies $\omega \ll 1/\tau_{\text{SF}}$, the parameter κ is real, and the phase of $\boldsymbol{\mu}_s(t)$ does not depend on the position x_1 . However, at the frequencies $\omega \sim 10 \text{ ns}^{-1}$ the spin accumulation $\boldsymbol{\mu}_s(x_1, t)$ has a position-dependent delay from the applied voltage $V(t)$.

Figure 11 shows the spatiotemporal map of the spin-accumulation component $\mu_2^s(x_1, t)$ generated in 5-μm-long n^+ -GaAs bar by the applied voltage with amplitude

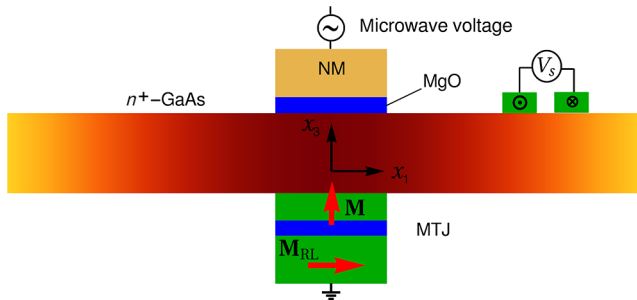


FIG. 10. Semiconducting GaAs bar sandwiched between electrically excited $\text{Co}_{20}\text{Fe}_{60}\text{B}_{20}$ /MgO/ $\text{Co}_{20}\text{Fe}_{60}\text{B}_{20}$ tunnel junction and MgO/metal bilayer. Information on the spin accumulation in GaAs can be obtained by measuring the voltage V_s between ferromagnetic nanocontacts with antiparallel magnetizations coupled to the bar surface.

$V_{\text{max}} = 800 \text{ mV}$ and frequency $f = 1.2 \text{ GHz}$. Since this frequency corresponds to the main peak of the magnetization precession, we assume that J_{32}^{SP} and μ_2 exhibit almost simple harmonic oscillations with the excitation frequency f . However, these oscillations lag behind the applied microwave voltage by about 0.25 ns at $|x_1| = L_{\text{SC}}/2$ in the 5-μm-long bar (see Fig. 11).

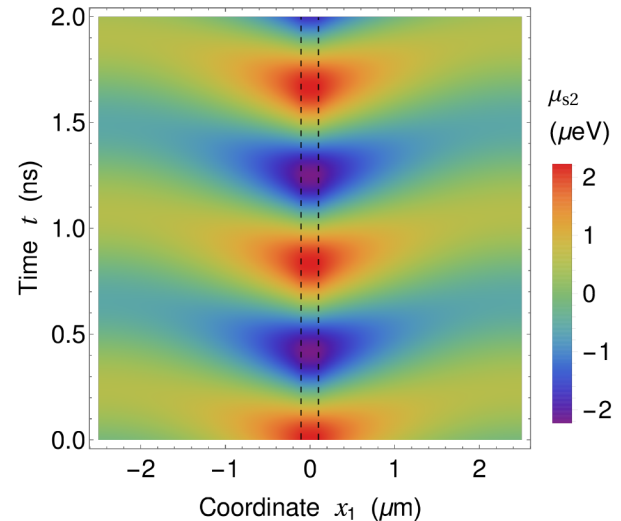


FIG. 11. Spatiotemporal map of the spin accumulation in the 5-μm-long n^+ -GaAs bar coupled to the electrically excited $\text{Co}_{20}\text{Fe}_{60}\text{B}_{20}$ /MgO/ $\text{Co}_{20}\text{Fe}_{60}\text{B}_{20}$ tunnel junction. The map gives the spin-accumulation component $\mu_2^s(x_1, t)$ generated by the microwave voltage with the amplitude $V_{\text{max}} = 800 \text{ mV}$ and frequency $f = 1.2 \text{ GHz}$. Vertical dashed lines indicate the surface region, where the bar is coupled to the junction's free layer.

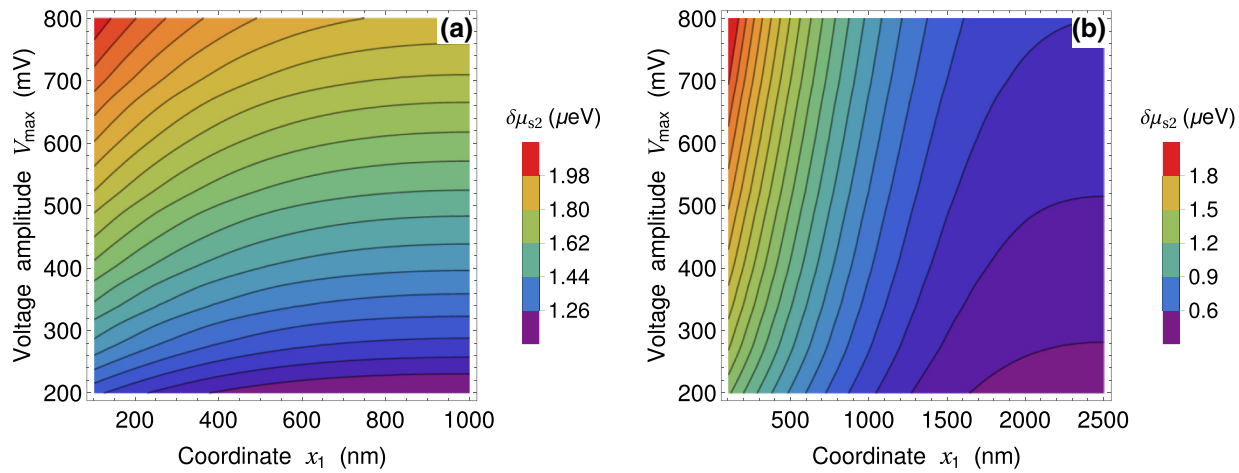


FIG. 12. Spin accumulation in the 2- μm -long (a) and 5- μm -long (b) n^+ -GaAs bars as a function of the spatial position x_1 and the amplitude V_{\max} of the microwave voltage applied to the heterostructure. The maps present the amplitude $\delta\mu_2^s(x_1)$ of the oscillating spin-accumulation component $\mu_2^s(x_1, t)$ calculated at the voltage-dependent resonance frequency $f_{\text{res}}(V_{\max})$. Lines show curves on which $\delta\mu_2^s$ remains constant.

The averaging of $\mu_2^s(x_1, t)$ over the oscillation period shows that the mean spin accumulation $\langle \mu_2^s(x_1) \rangle$ is negligible in comparison with the oscillation amplitude $\delta\mu_2^s(x_1)$. The maps presented in Fig. 12 demonstrate how the magnitude V_{\max} of applied microwave voltage influences the spatial distribution of $\delta\mu_2^s(x_1)$ calculated at the voltage-dependent resonance frequency $f_{\text{res}}(V_{\max})$. Remarkably, the ac component of the spin accumulation remains significant even at the ends of the considered GaAs bars with the length L_{SC} ranging from 2 to 5 μm . When L_{SC} is smaller

than the spin diffusion length $\lambda_{\text{SC}} = 2.32 \mu\text{m}$, $\delta\mu_2^s(x_1)$ appears to be weakly dependent on the coordinate x_1 near the bar ends [Fig. 12(a)]. In contrast, it decreases more rapidly with the distance from the bar center at $L_{\text{SC}} > \lambda_{\text{SC}}$ [Fig. 12(b)] and becomes smaller everywhere due to the spreading of nonequilibrium spin imbalance in a larger volume.

The spin accumulation in the GaAs bar can be measured experimentally by a method similar to a nonlocal detection of the spin injection into a normal conductor [3,68]. The method employs two ferromagnetic nanostrips integrated onto the bar surface and connected to a voltmeter (see Fig. 10). The nanostrips should be oriented along the x_2 axis and have antiparallel in-plane magnetizations. The presence of the spin accumulation $\mu_2^s(x_1, t)$ in the GaAs region beneath ferromagnetic strips with nanoscale widths of about 10 nm and small separation $\Delta x_1 \ll x_1$ manifests itself in a voltage $V_s(x_1, t) \propto \mu_2^s(x_1, t)$ between the nanocontacts. In the case of Fe nanocontacts forming Schottky tunnel barriers with n^+ -GaAs, $V_s(x_1, t) = \eta_{\text{IE}} p_{\text{Fe}} \mu_2^s(x_1, t) / e$, where $\eta_{\text{IE}} \approx 0.5$ is the spin transmission efficiency of the GaAs–Fe interface and $p_{\text{Fe}} \approx 0.42$ is the spin polarization of Fe at the Fermi level [68]. Using this relation, we calculate frequency spectra of the spin signals $V_s(x_1, t)$ generated in the 0.8- μm -long n^+ -GaAs bar at different excitation frequencies f . The map presented in Fig. 13 demonstrates amplitudes of the Fourier components of $V_s(t)$ determined at $V_{\max} = 800 \text{ mV}$ and the distance $|x_1| = 300 \text{ nm}$ from the bar center. It can be seen that the maximal ac spin signal with the amplitude of about 0.26 μV and frequency $f_s = f$ appears at the excitation frequencies $f = 1.2\text{--}1.4 \text{ GHz}$ close to the resonance frequency f_{res} . In addition, the Fourier components of $V_s(t)$ with frequencies f_s slightly above

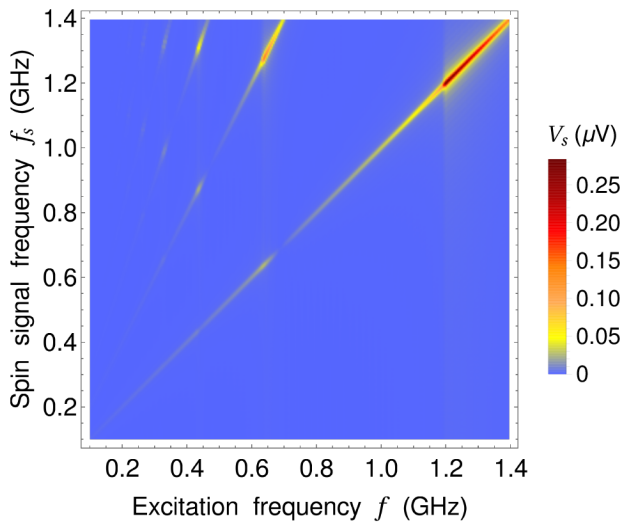


FIG. 13. Frequency spectra of the spin signals $V_s(t)$ generated in the 0.8- μm -long n^+ -GaAs bar at different excitation frequencies f . The map shows amplitudes of the Fourier components of $V_s(t)$ at the spatial position $x_1 = 300 \text{ nm}$. The applied voltage has the amplitude $V_{\max} = 800 \text{ mV}$, and its frequency increases from lower to higher values.

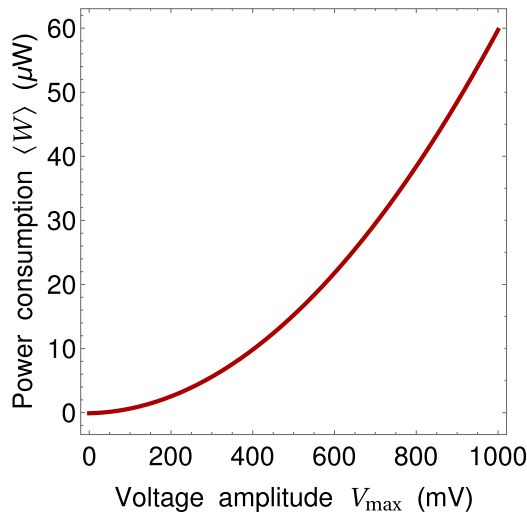


FIG. 14. Power consumption of the $\text{Co}_{20}\text{Fe}_{60}\text{B}_{20}/\text{MgO}/\text{Co}_{20}\text{Fe}_{60}\text{B}_{20}/\text{GaAs}/\text{MgO}$ heterostructure as a function of the amplitude of the applied microwave voltage.

f_{res} exhibit smaller maxima at the excitation frequencies $f \approx f_{\text{res}}/n$, which correspond to secondary peaks of the precession amplitude similar to those shown in Fig. 2(c). Remarkably, such spin signals have significant amplitudes ranging from $0.12 \mu\text{V}$ at $f \approx f_{\text{res}}/2$ to $0.04 \mu\text{V}$ at $f \approx f_{\text{res}}/3$, which can be detected experimentally. Thus, the proposed spin injector allows the generation of the ac spin accumulation in GaAs oscillating with the microwave frequency $f_s \approx f_{\text{res}}$ several times higher than the excitation frequency. Such frequency multiplication is promising for practical applications in spintronic devices, because frequency multipliers are widely used in electronics for increasing frequencies of electrical signals employed, e.g., in very high-speed computing, high-performance broadband communications, and mixer circuits [69]. It should be noted that the ac spin accumulation generated by the ac injector grows monotonically with increasing voltage amplitude V_{max} at any frequency f including those of secondary peaks. In contrast, the calculations show that the spin accumulation created in GaAs by the dc injector [58] vary nonmonotonically with increasing density of the applied direct current, being limited by some value. Hence the ac injector has an important advantage over the dc injector [58] for practical applications, with an additional benefit of almost linear variations of the ac spin accumulation with V_{max} below and above the threshold voltage V_{th} .

The mean power consumption $\langle W \rangle$ of the proposed spin injector can be estimated from the relation

$$\langle W \rangle = f L_1 L_2 \int_0^{1/f} J_c[t, m_1(t)] V_{\text{ac}}(t) dt, \quad (9)$$

where the integral is taken over the period of an applied ac voltage. Figure 14 shows the dependence $\langle W \rangle(V_{\text{max}})$ calculated for the $\text{Co}_{20}\text{Fe}_{60}\text{B}_{20}/\text{MgO}/\text{Co}_{20}\text{Fe}_{60}\text{B}_{20}/\text{GaAs}/\text{MgO}$ heterostructure considered in this work. It can be seen that $\langle W \rangle \propto V_{\text{max}}^2$ rises rapidly with the voltage amplitude, but remains well below $100 \mu\text{W}$ even at $V_{\text{max}} = 1 \text{ V}$. Hence the power dissipation of the electrically driven spin injector is more than 2 orders of magnitude smaller than that of the device excited by the microwave magnetic field (approximately 10 mW) [15].

V. CONCLUSIONS

In this paper, we theoretically describe the spin dynamics in the $\text{Co}_{20}\text{Fe}_{60}\text{B}_{20}/\text{MgO}/\text{Co}_{20}\text{Fe}_{60}\text{B}_{20}/\text{Au}$ and $\text{Co}_{20}\text{Fe}_{60}\text{B}_{20}/\text{MgO}/\text{Co}_{20}\text{Fe}_{60}\text{B}_{20}/\text{GaAs}$ heterostructures subjected to a microwave voltage. Our calculations are focused on the heterostructures comprising a nanoscale $\text{Co}_{20}\text{Fe}_{60}\text{B}_{20}/\text{MgO}/\text{Co}_{20}\text{Fe}_{60}\text{B}_{20}$ tunnel junction with an ultrathin FL having perpendicular magnetic anisotropy (Fig. 1). By solving the LLGS equation numerically, we first quantify the electrically induced precession of FL magnetization with the account of STT created by the spin-polarized current flowing through FL, VCMA associated with the FL–MgO interface, and enhanced Gilbert damping caused by the spin pumping into the overlayer. The calculated dependences of the precession amplitude on the frequency f and magnitude V_{max} of the applied voltage show that FL exhibits strongly nonlinear dynamic behavior at $V_{\text{max}} > 200 \text{ mV}$. In particular, the main peak of precession amplitude located at the resonance frequency f_{res} becomes asymmetric with a break on the left side [Fig. 2(b)], which is similar to the behavior of a Duffing oscillator with a softening nonlinearity [53]. At higher applied voltages $V_{\text{max}} > 500 \text{ mV}$, the frequency dependence of precession amplitude also involves strong secondary peaks and additional breaks [Fig. 2(c)].

The description of the magnetization dynamics occurring in the $\text{Co}_{20}\text{Fe}_{60}\text{B}_{20}$ FL enabled us to quantify the spin injection and pumping into the Au and GaAs overlayers. The total spin-current densities J_{3i}^s generated near the interface are calculated as a function of time at different frequencies and amplitudes of the applied voltage (Fig. 5). The analysis of these time dependences showed that the densities $J_{3i}^s(t)$ contain both ac and dc components, which mostly maximize under resonant excitation (Figs. 6 and 7). Interestingly, the ac components ΔJ_{31}^s and ΔJ_{32}^s also strongly increase at the excitation frequencies $f \approx f_{\text{res}}/2$ and high voltage amplitudes $V_{\text{max}} \geq 400 \text{ mV}$.

To evaluate the efficiency of spin generation in Au, we determine the distribution of electric potential in the 200-nm-thick Au overlayer by solving Laplace's equation. The charge current flowing in the overlayer is calculated with the account of the drift contribution and the inverse spin Hall effect. When finding the spatial distribution of

the actual spin-current density \mathbf{J}_{Au} we consider the spin injection and pumping at the FL-Au interface, spin relaxation and diffusion inside Au, and the spin backflow into FL. The calculated distribution of the electric potential ϕ is used to determine the transverse voltage $V_1(x_3) = \phi(x_1 = L_1, x_3) - \phi(x_1 = 0, x_3)$ between the sides of the Au overlayer normal to the x_1 axis parallel to the RL magnetization. It is found that both ac and dc components of this time-dependent voltage can be measured experimentally at small distances $x_3 < 30$ nm from the FL–Au interface under excitation by the microwave voltage with $f = f_{\text{res}}$ and $V_{\text{max}} = 600$ mV. The measured dependence $V_1(x_3)$ provides information on the spatial decay of the actual spin-current density J_{32}^{Au} reduced by spin backflow into FL and spin relaxation in Au.

In the final part of this study, we quantify the time-dependent spin accumulation in the n^+ -GaAs bar coupled to the Co₂₀Fe₆₀B₂₀/MgO/Co₂₀Fe₆₀B₂₀ junction at the center and separated from the NM lead by a thin MgO interlayer (Fig. 10). By solving numerically the spin-diffusion equation with appropriate boundary conditions, we calculate the spatiotemporal map of the spin-accumulation component $\mu_2^s(x_1, t)$ in the bar (Fig. 11). It is revealed that there is a position-dependent delay of $\mu_2^s(x_1, t)$ from the applied microwave voltage $V_{\text{ac}}(t)$. The time-averaged value $\langle \mu_2^s(x_1) \rangle$ of the oscillating spin accumulation is found to be negligible in comparison with the oscillation amplitude $\delta \mu_2^s(x_1)$. At the same time, the ac component $\delta \mu_2^s(x_1)$ of the spin accumulation under resonant excitation remains significant even at the ends of the 5-μm-long n^+ -GaAs bar. To detect this component, we propose to use two ferromagnetic nanostrips integrated onto the bar surface and connected to a voltmeter (Fig. 10). The voltage $V_s(x_1, t) \propto \mu_2^s(x_1, t)$ between such nanocontacts and its frequency spectrum are calculated. The results show that the maximal ac spin signal appears at the excitation frequencies $f = 1.2$ – 1.4 GHz close to the resonance frequency f_{res} . Its frequency f_s is equal to the excitation one, and the amplitude is about 0.26 μV at a representative distance $|x_1| = 300$ nm from the bar center. In addition, the Fourier components of $V_s(t)$ with frequencies f_s slightly above f_{res} exhibit significant maxima at the excitation frequencies about $f_{\text{res}}/2$ and $f_{\text{res}}/3$. These results demonstrate high efficiency of the described nanoscale spin injector and the possibility of ac spin accumulation with frequency multiplication. It should be noted that the proposed device is distinguished from the spin injector driven by a microwave magnetic field [15] by a compact design and low power consumption.

ACKNOWLEDGMENTS

This work is supported by the Foundation for the Advancement of Theoretical Physics and Mathematics “BASIS.”

- [1] I. Žutić, J. Fabian, and S. D. Sarma, Spintronics: Fundamentals and applications, *Rev. Mod. Phys.* **76**, 323 (2004).
- [2] H. Dery, P. Dalal, L. Cywinski, and L. J. Sham, Spin-based logic in semiconductors for reconfigurable large-scale circuits, *Nature* **447**, 573 (2007).
- [3] M. Johnson and R. H. Silsbee, Interfacial Charge-Spin Coupling: Injection and Detection of Spin Magnetization in Metals, *Phys. Rev. Lett.* **55**, 1790 (1985).
- [4] F. J. Jedema, A. T. Filip, and B. J. van Wees, Electrical spin injection and accumulation at room temperature in an all-metal mesoscopic spin valve, *Nature* **410**, 345 (2001).
- [5] G. Schmidt, D. Ferrand, L. W. Molenkamp, A. T. Filip, and B. J. van Wees, Fundamental obstacle for electrical spin injection from a ferromagnetic metal into a diffusive semiconductor, *Phys. Rev. B* **62**, R4790 (2000).
- [6] E. I. Rashba, Theory of electrical spin injection: Tunnel contacts as a solution of the conductivity mismatch problem, *Phys. Rev. B* **62**, R16267 (2000).
- [7] X. Jiang, R. Wang, R. M. Shelby, R. M. Macfarlane, S. R. Bank, J. S. Harris, and S. S. Parkin, Highly Spin-Polarized Room-Temperature Tunnel Injector for Semiconductor Spintronics Using MgO(100), *Phys. Rev. Lett.* **94**, 056601 (2005).
- [8] Y. Tserkovnyak, A. Brataas, G. E. W. Bauer, and B. I. Halperin, Nonlocal magnetization dynamics in ferromagnetic heterostructures, *Rev. Mod. Phys.* **77**, 1375 (2005).
- [9] A. Brataas, Y. Tserkovnyak, G. E. W. Bauer, and B. I. Halperin, Spin battery operated by ferromagnetic resonance, *Phys. Rev. B* **66**, 060404 (2002).
- [10] B. Heinrich, Y. Tserkovnyak, G. Woltersdorf, A. Brataas, R. Urban, and G. E. W. Bauer, Dynamic Exchange Coupling in Magnetic Bilayers, *Phys. Rev. Lett.* **90**, 187601 (2003).
- [11] E. Saitoh, M. Ueda, H. Miyajima, and G. Tatara, Conversion of spin current into charge current at room temperature: Inverse spin-Hall effect, *Appl. Phys. Lett.* **88**, 182509 (2006).
- [12] O. Mosendz, V. Vlaminck, J. E. Pearson, F. Y. Fradin, G. E. W. Bauer, S. D. Bader, and A. Hoffmann, Detection and quantification of inverse spin Hall effect from spin pumping in permalloy/normal metal bilayers, *Phys. Rev. B* **82**, 214403 (2010).
- [13] C. W. Sandweg, Y. Kajiwara, K. Andoa, E. Saitoh, and B. Hillebrands, Enhancement of the spin pumping efficiency by spin wave mode selection, *Appl. Phys. Lett.* **97**, 252504 (2010).
- [14] K. Ando, S. Takahashi, J. Ieda, Y. Kajiwara, H. Nakayama, T. Yoshino, K. Harii, Y. Fujikawa, M. Matsuo, S. Maekawa, and E. Saitoh, Inverse spin-Hall effect induced by spin pumping in metallic system, *J. Appl. Phys.* **109**, 103913 (2011).
- [15] K. Ando, S. Takahashi, J. Ieda, H. Kurebayashi, T. Trypiniotis, C. H. W. Barnes, S. Maekawa, and E. Saitoh, Electrically tunable spin injector free from the impedance mismatch problem, *Nat. Mat.* **10**, 655 (2011).
- [16] E. Shikoh, K. Ando, K. Kubo, E. Saitoh, T. Shinjo, and M. Shiraishi, Spin-Pump-Induced Spin Transport in p-Type Si at Room Temperature, *Phys. Rev. Lett.* **110**, 127201 (2013).
- [17] S. I. Kiselev, J. C. Sankey, I. N. Krivorotov, N. C. Emley, R. J. Schoelkopf, R. A. Buhrman, and D. C. Ralph, Microwave

- oscillations of a nanomagnet driven by a spin-polarized current, *Nature (London)* **425**, 380 (2003).
- [18] A. A. Tulapurkar, Y. Suzuki, A. Fukushima, H. Kubota, H. Maehara, K. Tsunekawa, D. D. Djayaprawira, N. Watanabe, and S. Yuasa, Spin-torque diode effect in magnetic tunnel junctions, *Nature (London)* **438**, 339 (2005).
- [19] J. C. Sankey, P. M. Braganca, A. G. F. Garcia, I. N. Krivorotov, R. A. Buhrman, and D. C. Ralph, Spin-Transfer-Driven Ferromagnetic Resonance of Individual Nanomagnets, *Phys. Rev. Lett.* **96**, 227601 (2006).
- [20] M. Deac, A. Fukushima, H. Kubota, H. Maehara, Y. Suzuki, S. Yuasa, Y. Nagamine, K. Tsunekawa, D. D. Djayaprawira, and N. Watanabe, Bias-driven high-power microwave emission from MgO-based tunnel magnetoresistance devices, *Nat. Phys.* **4**, 803 (2008).
- [21] G. Bertotti, C. Serpico, I. D. Mayergoyz, R. Bonin, and M. d'Aquino, Current-induced magnetization dynamics in nanomagnets, *J. Magn. Magn. Mater.* **316**, 285 (2007).
- [22] T. Nozaki, Y. Shiota, S. Miwa, S. Murakami, F. Bonell, S. Ishibashi, H. Kubota, K. Yakushiji, T. Saruya, A. Fukushima, S. Yuasa, T. Shinjo, and Y. Suzuki, Electric-field-induced ferromagnetic resonance excitation in an ultrathin ferromagnetic metal layer, *Nat. Phys.* **8**, 491 (2012).
- [23] J. Zhu, J. A. Katine, G. E. Rowlands, Y.-J. Chen, Z. Duan, J. G. Alzate, P. Upadhyaya, J. Langer, P. K. Amiri, K. L. Wang, and I. N. Krivorotov, Voltage-Induced Ferromagnetic Resonance in Magnetic Tunnel Junctions, *Phys. Rev. Lett.* **108**, 197203 (2012).
- [24] G. Viaud and N. A. Pertsev, Dynamic converse magnetoelectric effect in ferromagnetic nanostructures with electric-field-dependent interfacial anisotropy, *Phys. Rev. B* **90**, 064429 (2014).
- [25] K. Miura, S. Yabuuchi, M. Yamada, M. Ichimura, B. Rana, S. Ogawa, H. Takahashi, Y. Fukuma, and Y. Otani, Voltage-induced magnetization dynamics in CoFeB/MgO/CoFeB magnetic tunnel junctions, *Sci. Rep.* **7**, 42511 (2017).
- [26] M. Weiler, L. Dreher, C. Heeg, H. Huebl, R. Gross, M. S. Brandt, and S. T. B. Goennenwein, Elastically Driven Ferromagnetic Resonance in Nickel Thin Films, *Phys. Rev. Lett.* **106**, 117601 (2011).
- [27] M. Weiler, H. Huebl, F. S. Goerg, F. D. Czeschka, R. Gross, and S. T. B. Goennenwein, Spin Pumping with Coherent Elastic Waves, *Phys. Rev. Lett.* **108**, 176601 (2012).
- [28] A. V. Azovtsev and N. A. Pertsev, Magnetization dynamics and spin pumping induced by standing elastic waves, *Phys. Rev. B* **94**, 184401 (2016).
- [29] N. I. Polzikova, S. G. Alekseev, V. A. Luzanov, and A. O. Raevskiy, Electroacoustic excitation of spin waves and their detection due to the inverse spin hall effect, *Phys. Solid State* **60**, 2211 (2018).
- [30] A. V. Azovtsev and N. A. Pertsev, Dynamical spin phenomena generated by longitudinal elastic waves traversing CoFe₂O₄ films and heterostructures, *Phys. Rev. B* **100**, 224405 (2019).
- [31] Y. Tserkovnyak, A. Brataas, and G. E. W. Bauer, Enhanced Gilbert Damping in Thin Ferromagnetic Films, *Phys. Rev. Lett.* **88**, 117601 (2002).
- [32] J. C. Slonczewski, Conductance and exchange coupling of two ferromagnets separated by a tunneling barrier, *Phys. Rev. B* **39**, 6995 (1989).
- [33] J. C. Slonczewski and J. Z. Sun, Theory of voltage-driven current and torque in magnetic tunnel junctions, *J. Magn. Magn. Mater.* **310**, 169 (2007).
- [34] S. Ikeda, K. Miura, H. Yamamoto, K. Mizunuma, H. D. Gan, M. Endo, S. Kanai, J. Hayakawa, F. Matsukura, and H. Ohno, A perpendicular-anisotropy CoFeB-MgO magnetic tunnel junction, *Nat. Mater.* **9**, 721 (2010).
- [35] S. Kanai, M. Yamanouchi, S. Ikeda, Y. Nakatani, F. Matsukura, and H. Ohno, Electric field-induced magnetization reversal in a perpendicular-anisotropy CoFeB-MgO magnetic tunnel junction, *Appl. Phys. Lett.* **101**, 122403 (2012).
- [36] D. V. Berkov and J. Miltat, Spin-torque driven magnetization dynamics: Micromagnetic modeling, *J. Magn. Magn. Mater.* **320**, 1238 (2008).
- [37] B. Fang, M. Carpentieri, X. Hao, H. Jiang, J. A. Katine, I. N. Krivorotov, B. Ocker, J. Langer, K. L. Wang, B. Zhang, B. Azzerboni, P. K. Amiri, G. Finocchio, and Z. Zeng, Giant spin-torque diode sensitivity in the absence of bias magnetic field, *Nat. Commun.* **7**, 11259 (2016).
- [38] M. Zwierzycki, Y. Tserkovnyak, P. J. Kelly, A. Brataas, and G. E. W. Bauer, First-principles study of magnetization relaxation enhancement and spin transfer in thin magnetic films, *Phys. Rev. B* **71**, 064420 (2005).
- [39] A. Slavin and V. Tiberkevich, Nonlinear auto-oscillator theory of microwave generation by spin-polarized current, *IEEE Trans. Magn.* **45**, 1875 (2009).
- [40] S. Ikeda, R. Koizumi, H. Sato, M. Yamanouchi, K. Miura, K. Mizunuma, H. Gan, F. Matsukura, and H. Ohno, Boron composition dependence of magnetic anisotropy and tunnel magnetoresistance in MgO/CoFe(B) based stack structures, *IEEE Trans. Magn.* **48**, 3829 (2012).
- [41] J. G. Alzate, P. K. Amiri, G. Yu, P. Upadhyaya, J. A. Katine, J. Langer, B. Ocker, I. N. Krivorotov, and K. L. Wang, Temperature dependence of the voltage-controlled perpendicular anisotropy in nanoscale MgO-CoFeB-Ta magnetic tunnel junctions, *Appl. Phys. Lett.* **104**, 112410 (2014).
- [42] M. K. Niranjan, C.-G. Duan, S. S. Jaswal, and E. Y. Tsymbal, Electric field effect on magnetization at the Fe/MgO(001) interface, *Appl. Phys. Lett.* **96**, 222504 (2010).
- [43] A. Aharoni, Demagnetizing factors for rectangular ferromagnetic prisms, *J. Appl. Phys.* **83**, 3432 (1998).
- [44] K. Lee, J. J. Sapan, S. H. Kang, and E. E. Fullerton, Perpendicular magnetization of CoFeB on single-crystal MgO, *Appl. Phys. Lett.* **109**, 123910 (2011).
- [45] R. C. Hall, Magnetic anisotropy and magnetostriction of ordered and disordered Cobalt-iron alloys, *J. Appl. Phys.* **31**, S157–S158 (1960).
- [46] K. Tsunekawa, M. Nagai, H. Maehara, S. Yamagata, D. D. Djayaprawira, N. Watanabe, S. Yuasa, Y. Suzuki, and K. Ando, in *2005 IEEE International Magnetics Conference (INTERMAG), Nagoya, Japan, 4–8 April 2005* (IEEE, Piscataway, NJ, 2005), p. 1223.
- [47] S. X. Huang, T. Y. Chen, and C. L. Chien, Spin polarization of amorphous CoFeB determined by point-contact Andreev reflection, *Appl. Phys. Lett.* **92**, 242509 (2008).
- [48] W. Skowroński, T. Stobiecki, J. Wrona, K. Rott, A. Thomas, G. Reiss, and S. van Dijken, Interlayer exchange coupling and current induced magnetization switching in magnetic

- tunnel junctions with MgO wedge barrier, *J. Appl. Phys.* **107**, 093917 (2010).
- [49] S. Peng, W. Zhao, J. Qiao, L. Su, J. Zhou, H. Yang, Q. Zhang, Y. Zhang, C. Grezes, P. K. Amiri, and K. L. Wang, Giant interfacial perpendicular magnetic anisotropy in MgO/CoFe/capping layer structures, *Appl. Phys. Lett.* **110**, 072403 (2017).
- [50] J. Fontanella, C. Andeen, and D. Schuele, Low-frequency dielectric constants of α -quartz, sapphire, MgF_2 , and MgO, *J. Appl. Phys.* **45**, 2852 (1974).
- [51] M. Goto, Y. Wakatake, U. K. Oji, S. Miwa, N. Strelkov, B. Dieny, H. Kubota, K. Yakushiji, A. Fukushima, S. Yuasa, and Y. Suzuki, Microwave amplification in a magnetic tunnel junction induced by heat-to-spin conversion at the nanoscale, *Nat. Nanotech.* **4**, 40 (2019).
- [52] H. Jiao and G. E. W. Bauer, Spin Backflow and ac Voltage Generation by Spin Pumping and the Inverse Spin Hall Effect, *Phys. Rev. Lett.* **110**, 217602 (2013).
- [53] A. H. Nayfeh and D. T. Mook, *Nonlinear Oscillations* (Wiley, New York, 1979).
- [54] W. Chen, G. de Loubens, J.-M. L. Beaujour, J. Z. Sun, and A. D. Kent, Spin-torque driven ferromagnetic resonance in a nonlinear regime, *Appl. Phys. Lett.* **95**, 172513 (2009).
- [55] O. V. Prokopenko, I. N. Krivorotov, E. Bankowski, T. Meitzler, S. Jaroch, V. S. Tiberkevich, and A. N. Slavin, Spin-torque microwave detector with out-of-plane precessing magnetic moment, *J. Appl. Phys.* **111**, 123904 (2012).
- [56] B. Rana, Y. Fukuma, K. Miura, H. Takahashi, and Y. Otani, Effect of excitation power on voltage induced local magnetization dynamics in an ultrathin CoFeB film, *Sci. Rep.* **7**, 2318 (2017).
- [57] Y. Jia, S. Du, and A. A. Seshia, Twenty-eight orders of parametric resonance in a microelectromechanical device for multi-band vibration energy harvesting, *Sci. Rep.* **6**, 30167 (2016).
- [58] A. I. Nikitchenko and N. A. Pertsev, Spin injection and pumping generated by a direct current flowing through a magnetic tunnel junction, *Phys. Rev. B* **99**, 224426 (2019).
- [59] M. I. Dyakonov and V. I. Perel, Current-induced spin orientation of electrons in semiconductors, *Phys. Lett. A* **35**, 459 (1971).
- [60] Y. Tserkovnyak and A. Brataas, Spin pumping and magnetization dynamics in metallic multilayers, *Phys. Rev. B* **66**, 224403 (2002).
- [61] W. M. Haynes, *CRC Handbook of Chemistry and Physics*, 95th ed. (CRC Press, Boca Raton, FL, 2014).
- [62] O. Mosendz, J. E. Pearson, F. Y. Fradin, G. E. W. Bauer, S. D. Bader, and A. Hoffmann, Quantifying Spin Hall Angles from Spin Pumping: Experiments and Theory, *Phys. Rev. Lett.* **104**, 046601 (2010).
- [63] S. Takahashi and S. Maekawa, Spin injection and detection in magnetic nanostructures, *Phys. Rev. B* **67**, 052409 (2003).
- [64] J. M. Kikkawa and D. D. Awschalom, Resonant Spin Amplification in *n*-Type GaAs, *Phys. Rev. Lett.* **80**, 4313 (1998).
- [65] X. Fan, H. Celik, J. Wu, C. Ni, K.-J. Lee, V. O. Lorenz, and J. Q. Xiao, Quantifying interface and bulk contributions to spin-orbit torque in magnetic bilayers, *Nat. Commun.* **5**, 3042 (2003).
- [66] S. G. Bhat and P. S. A. Kumar, Room temperature electrical spin injection into GaAs by an oxide spin injector, *Sci. Rep.* **4**, 5588 (2014).
- [67] G. Zahnd, L. Vila, V. T. Pham, M. Cosset-Cheneau, W. Lim, A. Brenac, P. Laczkowski, A. Marty, and J. P. Attané, Spin diffusion length and polarization of ferromagnetic metals measured by the spin-absorption technique in lateral spin valves, *Phys. Rev. B* **98**, 174414 (2018).
- [68] X. Lou, C. Adelmann, S. A. Crooker, E. S. Garlid, J. Zhang, K. S. M. Reddy, S. D. Flexner, C. J. Palmstrøm, and P. A. Crowell, Electrical detection of spin transport in lateral ferromagnet–semiconductor devices, *Nat. Phys.* **3**, 197 (2007).
- [69] C. E. Saavedra, in *CMOS Nanoelectronics: Analog and RF VLSI Circuits* (Queen's University, Kingston, Ontario, Canada, 2018), Chap. 5.